



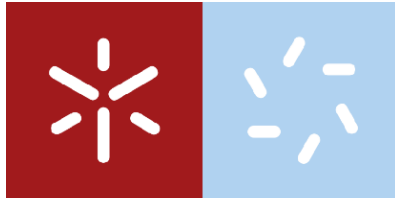
Universidade do Minho
Escola de Ciências

Development of nanostructured thin films
for humidity and temperature sensors

João Paulo Carmo da Silva

João Paulo Carmo da Silva

Development of nanostructured thin
films for humidity and temperature
sensors



Universidade do Minho

Escola de Ciências

João Paulo Carmo da Silva

**Development of nanostructured thin films for
humidity and temperature sensors**

Dissertação de Mestrado

Mestrado em Física

Trabalho efetuado sob a orientação de

Doutor Armando Ferreira

Doutora Daniela Correia

fevereiro 2021

Direitos de autor e condições de utilização do trabalho por terceiros

Este é um trabalho académico que pode ser utilizado por terceiros desde que respeitadas as regras e boas práticas internacionalmente aceites, no que concerne aos direitos de autor e direitos conexos.

Assim, o presente trabalho pode ser utilizado nos termos previstos na licença [abaixo](#) indicada.

Caso o utilizador necessite de permissão para poder fazer um uso do trabalho em condições não previstas no licenciamento indicado, deverá contactar o autor, através do RepositóriUM da Universidade do Minho.

Licença concedida aos utilizadores deste trabalho



**Atribuição
CC BY**

<https://creativecommons.org/licenses/by/4.0/>

Acknowledgements

During these past 18 months, many were those who contributed in some way to the development of these master's thesis, and for those people, which I must express my gratitude for all that they represented.

To Doctor Armando Ferreira and Dra. Daniela Correia for the amazing help, counselling, patience and friendship that they were able to provide me.

To the Electroactive Smart Materials Group where I was integrated for making me feel welcomed and for the help that they never denied me and specifically to engineer Nelson Pereira for all the help that he gave me.

To Professor Felipe Vaz and to Professor Marcio Correa for the contributions given in the publication of the articles that served as the background of this document.

To the GRFVAZ for providing the PVD equipment and the means to produce the thin films presented on this thesis.

To the University of Minho, especially to the Centre of Physics for providing means to produce the work presented on this thesis, on such challenging times.

To my family for the love and the support they gave along the years and through this thesis development.

To my friends, for their friendship since one cannot do this path alone.

And last, but not least, to all those who helped me get through some personal problems that appeared along with this master thesis development, some of those people already mentioned here.

To all of you, a sincere Thank you

Statement of integrity

I hereby declare having conducted this academic work with integrity. I confirm that I have not used plagiarism or any form of undue use of information or falsification of results along the process leading to its elaboration.

I further declare that I have fully acknowledged the Code of Ethical Conduct of the University of Minho.

Resumo

Este trabalho visa apresentar todo o processo de produção e resposta de um conjunto de filmes finos multifuncionais com capacidade de sensorização de temperatura e/ou de humidade relativa produzidos através da técnica de deposição física em fase de vapor (*Physical Vapor Deposition*, PVD) com auxílio do sistema *Glancing Angle Deposition* - GLAD. Neste sentido, foram preparados dois conjuntos de filmes finos: filmes de nitreto de crómio (CrN) e oxinitreto de crómio (CrN_xO_y). Durante a preparação dos filmes nanoestruturados em ziguezague, foi variada a quantidade de oxigénio e azoto com a finalidade de se obter uma variação na resposta elétrica quando sujeitos a uma variação de temperatura ou humidade relativa. Os filmes produzidos foram sujeitos a diferentes técnicas de caracterização com o intuito de avaliar as propriedades estruturais, morfológicas e elétricas.

Para os sensores de temperatura foram usados os filmes finos de CrN_x, nos quais, as técnicas de difração raio-X e de microscopia eletrónica de varrimento permitiram a avaliação das propriedades estruturais e morfológicas das amostras de CrN_x em função do fluxo de N₂ durante a deposição. Efetuou-se um estudo sistemático do efeito termorresistivo dos filmes finos de CrN_x, de modo a determinar o coeficiente de resistência de temperatura (TCR). A resposta termorresistiva foi avaliada medindo a resistividade elétrica em função da temperatura através do método de duas pontas. Os filmes finos depositados com um fluxo de N₂ entre os 4 e os 8 sccm apresentaram um TCR negativo, com uma variação de $9.18 \times 10^{-4} \pm 2.47 \times 10^{-6} \text{ } ^\circ\text{C}^{-1}$ até $1.48 \times 10^{-2} \pm 1.74 \times 10^{-5} \text{ } ^\circ\text{C}^{-1}$ e uma resposta elétrica estável ao longo do tempo para diferentes estágios de temperaturas. O modelo teórico de fronteira de grão foi usado para descrever os resultados experimentais obtidos.

Para os sensores de humidade foram utilizados os filmes finos de CrN_xO_y. Os resultados obtidos demonstraram que com o aumento de oxigénio, à medida que o fluxo da mistura N₂+O₂ aumenta, ocorre uma transição de fase de nitreto de crómio para óxido de crómio. Ao mesmo tempo ocorre uma mudança na estrutura cristalina de cubica de corpo centrado do crómio (BCC-Cr) para uma estrutura cubica de face centrada (FCC-CrN). A quantidade de O₂ presente na composição dos revestimentos faz com que exista um aumento da resistência elétrica, variando de $1.27 \times 10^{-6} \pm 5.02 \times 10^{-8} \text{ } \Omega \cdot \text{m}$ para a amostra com uma percentagem atómica de O₂ de 16 % até $4.50 \times 10^{-9} \pm 4.20 \times 10^{-7} \text{ } \Omega \cdot \text{m}$ para a amostra com uma percentagem atómica de O₂ de 60 %. A maior resposta do transdutor à variação de humidade relativa

(RH) entre 40 % e 80 % foi de $1.87 \times 10^{-2} \pm 7.00 \times 10^{-5} \text{ (RH\%)}^{-1}$. Os resultados obtidos demonstram o potencial de CrN_x e de CrN_xO_y para aplicações de sensorização.

Palavras chave: Revestimentos duros multifuncionais; pulverização catódica em corrente contínua; Coeficiente de Resistência de temperatura; propriedades térmicas; sensorização de temperatura; nitreto de crômio; Oxinitreto de crômio; Humidade relativa; sensorização de humidade.

Abstract

This work aims to present the entire production and response process of a set of multifunctional films capable of sensing temperature or relative humidity produced using the Physical Vapor Deposition, (PVD) with the assistance of the Glancing Angle Deposition technique - GLAD. In this work, two sets of thin films were prepared (chromium nitride (CrN) and chromium oxynitride (CrN_xO_y) grown with a zigzag like nanostructure, varying the amount of nitrogen and oxygen in order to obtain a variation in the electrical response when subjected to a variation in temperature or relative humidity. The films produced were analyzed by different characterization techniques in order to evaluate their structural, morphological and electrical properties.

In order to obtain thin films with the capability to sense variations in temperature, a systematic study of the thermo-resistive effect of chromium nitride (CrN_x) thin films with negative temperature coefficient of resistance (TCR) has been carried out. A systematic study of the thermoresistive effect of chromium nitride (CrN_x) thin films with negative temperature coefficient of resistance (TCR) has been carried out. CrN_x nanostructures were grown by reactive magnetron sputtering, with oblique angle deposition, under distinct Ar+N₂ conditions. This experimental setup enables to confer a zigzag columnar morphology to the CrN_x thin films and thus modify the structural, morphological and physical properties of the samples. X-ray diffraction and Scanning Electron Microscopy allowed to evaluate the evolution of the structural and morphological properties of the samples as a function of the N₂ flux during the deposition. The thermo-resistive response was evaluated by measuring the electrical resistivity as a function of temperature by the two-point method. The thin films with N₂ flux between 4 and 8 sccm presented a negative TCR with values ranging from $9.18 \times 10^{-4} \pm 2.47 \times 10^{-6} \text{ }^{\circ}\text{C}^{-1}$ to $1.48 \times 10^{-2} \pm 1.74 \times 10^{-5} \text{ }^{\circ}\text{C}^{-1}$, respectively, and a very stable time response at a given temperature. The grain-boundary model was used to describe the experimental results and, in particular, the negative TCR values of the samples.

In order to obtain thin films with relative humidity sensing capability, thin films based on chromium oxynitride (CrN_xO_y) were prepared with zigzag nanostructures and varying the amount of nitrogen and oxygen in order to enhance the humidity response. The obtained CrN_xO_y thin films show an increasing amount of oxygen as the N₂+O₂ mixture flux increased, leading to a transition from chromium nitride to chromium oxide. Further, a change from a BCC-Cr to a pure FCC-CrN phase is obtained as the oxygen in the sample increases. The amount of oxygen present in the composition of the coating leads to high

electrical resistivity, ranging from $1.27 \times 10^6 \pm 5.02 \times 10^8 \, \Omega \cdot \text{m}$ for the sample with 16 at.% of O_2 to $4.50 \times 10^9 \pm 4.20 \times 10^7 \, \Omega \cdot \text{m}$ for the sample with 60 at.% of O_2 . The highest sensibility to the relative humidity (RH) variation from 40 % to 80 % was $1.87 \times 10^{-2} \pm 7.00 \times 10^{-5} \, (\text{RH}\%)^{-1}$. The obtained results demonstrate the potential of CrN_x and of CrN_xO_y for sensor applications.

Keywords: Multifunctional hard coatings; DC sputtering; Temperature Coefficient of Resistance; Thermal properties; Temperature sensing; Chromium nitride; Chromium oxynitride; Relative Humidity; Humidity sensing.

Table of Contents

Resumo.....	v
Abstract.....	vii
List of Figures.....	xi
List of Tables.....	xiii
List of abbreviations.....	xiv
1. Introduction	1
1.1. Thin films based on chromium	2
1.2. Main goal of the work	3
1.3. Thesis structure	3
2. State-of-the-Art.....	5
2.1. Temperature sensors	5
2.2. Relative humidity sensors	7
3. Experimental details	10
3.1.1. The magnetron sputtering technique	10
3.1.1.1. GLancing Angle Deposition - GLAD	11
3.1.1.2. Deposition conditions.....	12
3.1.2. Morphological, composition and structural characterization	13
3.1.2.1. Scanning electron microscopy – SEM.....	13

3.1.2.2.	Rutherford Backscattering Spectrometry.....	14
3.1.2.3.	X-ray diffraction measurements	15
3.1.3.	Electrical, thermoresistive and relative humidity measurements.....	17
3.1.3.1.	Electrical resistive measurements.....	17
3.1.3.2.	Thermoresistive measurements.....	17
3.1.3.3.	Relative humidity measurements.....	19
4.	Results and discussion	20
4.1.	Temperature sensor results.....	20
4.1.1.	Structural and Morphological Characterization.....	20
4.1.2.	Electrical and thermo-resistive measurements.....	24
4.1.3.	Grain-boundary model	27
4.2.	Relative humidity sensor.....	30
4.2.1.	Morphological and Structural Characterization.....	30
4.2.2.	Electrical properties	34
4.2.3.	Relative Humidity Sensing Characteristics	35
5.	Conclusions	38
6.	Future work.....	40
7.	References	41

List of Figures

Figure 1: Schematic diagram of the Oblique Angle Deposition set-up. α is the applied angle of the substrate relative to the Cr particle flux, β is the column growth angle, and Φ is the angular direction...	2
Figure 2: Some thermistors shapes and sizes [43].	6
Figure 3: Nuclear processes during the sputtering process.	10
Figure 4: Vacuum chamber used in this work.	11
Figure 5: Schematic diagram of the GLAD Deposition set-up. α is the applied angle of the substrate relative to the Cr particle flux, β is the column growth angle, and Φ is the angular direction.	12
Figure 6: XRD schematization, the detector and X-ray source move by $-\theta$ and by θ providing the 2θ measurement.	15
Figure 7: Bragg law a) X-rays diffracting on the sample atoms, b) path-length difference.	16
Figure 8: Schematic representation of the thermoresistive setup.	18
Figure 9: Schematic representation of the humidity chamber setup using a hermetic vapor chamber (P-Selecta) with temperature control.	19
Figure 10: X-ray diffraction diagrams for the Cr and CrN samples. The peaks are indexed by using the ICSD card nos. 00-900-8619 and 00-003-1191 for CrN and Cr_2N , respectively.	21
Figure 11: (a) Texture coefficient $T_{c(hkl)}$ variations of the CrN thin films at different N_2 concentrations. (b) Grains size of the films as a function of N_2 concentrations obtained from the XRD results.	22
Figure 12: Representative SEM micrographs of the Cr samples, (a) Cr cross section, (b),(c) and (d) top view of the Cr, CrN-4sccm, and CrN-8sccm samples, respectively.	23
Figure 13: Temperature dependent electrical resistivity over time. (a) Results for the N_2 flux of 4 sccm. (b) Zoomed range of the sample deposited with a N_2 flux of 4 sccm. (c) N_2 flux of 6 sccm. (d) Zoomed curves for N_2 flux of 6 sccm. (e) Results for the samples deposited with N_2 flux of 8 sccm. (f) Zoomed curves for N_2 flux of 8 sccm.	25

Figure 14: Evolution of the electrical resistivity and temperature coefficient of resistance as a function of the N_2 flux during sample preparation.....	26
Figure 15: (a) ρ_G as a function of the temperature for distinct values of the grain-size (D_s). For this calculation, the following parameters are considered: $\rho = 1.04$, $S = 0.13$, $n = 40.4 \times 10^{23}$, and $\chi = 0.21 \times 10^4$ nm. (b) Similar plot for $D_s = 2.21$ nm and distinct values of L_{ESM} . (c) Electrical resistivity measured for the CrN samples growth onto 8 (Blue), 6 (Red) and 4 (Black) sccm N_2 flux. The red line indicates the best fit, calculated from the grain-boundary model. The parameters used in this fit are shown in Tab.2.	28
Figure 16: Representative SEM micrographs of the CrN_xO_y samples: a), c) and e) are the cross section views and b), d) and f) top views of the samples with N_2+O_2 flux of 0, 4 and 10 sccm, respectively.	30
Figure 17: a) Deposition rate and b) elementary composition variation as a function of the N_2+O_2 flux..	32
Figure 18: X-ray diffraction spectra of the CrN_xO_y samples.....	33
Figure 19: Room temperature resistivity, grain size and amount of O_2 as a function of the N_2+O_2 reactive flux.	34
Figure 20: Sensor response characterization by the electrical resistance variation with the relative humidity for the samples deposited with a flux of N_2+O_2 of: a) 4 sccm, c) 10 sccm and the corresponding magnifications b) and d) for a single cycle.	35
Figure 21: a) Electrical resistivity and ΔRH as a function of the N_2+O_2 flow rate applied during the reactive sputtering of the CrN_xO_y samples, b) adsorbed layers on a high humidity environment.	36

List of Tables

Table 1: Characteristics of the most widely applied temperature sensors, platinum RTDs, thermocouples and thermistors, adapted from [40].....	6
Table 2: Capacitive and resistive humidity sensors comparison [52].....	7
Table 3: Advantages and disadvantages of resistive humidity sensors made from different materials [4,48,52].....	8
Table 4: Metal oxides used on resistive humidity sensors adapted from [4]	9
Table 5: Varying conditions of the depositions	13
Table 6: Elemental composition of the CrN samples.....	21
Table 7: Parameters employed in the scope of the grain-boundary model to describe the electrical resistivity depicted in the Fig.15. β_G ($10^{-3}K^{-1}$) values are obtained/calculated at room temperature (293 K).....	29

List of abbreviations

A – Ampers

Å – Angstrom

A_c – Area of contact

BCC – Body-centered cubic

Cr – Chromium

CrN – Chromium nitride

CrN_xO_y – Chromium oxynitride

Cr₂O₃ – Chromium oxide

DR – deposition rate

dc – Direct current

EDS – Energy-dispersive x-ray spectroscopy

FCC – Face-centered cubic

GLAD – glancing angle deposition

K – Kelvin

NTC – Negative temperature coefficient (of resistance)

PVD – Physical vapor deposition

PTC – Positive temperature coefficient (of resistance)

RTD – Resistance temperature detector

RBS – Rutherford backscattering spectrometry

SEM – Scanning electron microscopy

sccm – Standard cubic centimetre per minute

TCR – Temperature coefficient of resistance

V – Volts

XRD – X-ray diffraction

1. Introduction

The introduction of this work aims to contextualize and indicate reasons for the importance of this study, the entire process which involve the production of thin films by PVD techniques and their characterization in terms of physical, chemical and thermal properties, in order to assess its applicability and functionality.

Since the industrial revolution, the industry has had a growing need to control production variables, such as temperature, pressure and humidity [1]. This necessity was further increased with the beginning of the fourth industrial revolution, denominated by Industry 4.0 [2]. Industry 4.0 is inherently a symbol of connectivity between things and people throughout the manufacturing process. Some of the goals for Industry 4.0 are quite ambitious, the hope is that it can evolve into artificial intelligence and automated decision-making, near-perfect mechanical automation and symbiotic human integration, and have manufacturing facilities that are completely interconnected and 'smart', from raw materials to finished goods. While this change may seem overwhelming, it can be achieved by working incrementally, starting small by identifying pain points of facilities and scaling when success is shown [2].

Manufacturers are able to make strides toward Industry 4.0 through three pillars of thought: digitization, sensorization and optimization. This work is based on the second industry pillar of thought: the sensorization. Sensors are cost-effective ways to measure and control production variables, in this new production standardization. Control devices and industrial machinery should be able to make decentralized decisions in order to control the production in a semi-independent way [2]. These decisions are adapted to the manufacturing process variables since the quality and the economic viability of the product will be affected by the production conditions [3]. Therefore, sensors should not only have a good sensibility to the intended variable, but also, they should have stability [4], durability [4], reduced size [4], easily transferable results [4], low price and be able to be applicable in different environments [4]. For that, the development of a skin-like thin film needs to be optimized according to the basic requirements of each kind of sensing [5,6].

For the development of functional and multifunctional thin films, Physical Vapor Deposition (PVD) is one of the preferred techniques as it allows the control of the process parameters and stoichiometry of the deposited coatings [7]. The synergy between PVD technologies and Glancing Angle Deposition (GLAD) has attracted increasing interest due to the precise control of the microstructural (isotropic and anisotropic) and physical-chemical properties [8]. The GLAD takes the advantage of the shadowing effect and diffusion of the particles on

the growing film [9]. The basic features of this deposition technique consist in depositing thin films under an oblique incident flux of the sputtered particles, using a mobile substrate (Fig. 1). In the columnar films, the substrate holder was static, while for the zigzag coatings the substrate was periodically rotated in the Φ direction. The growth of thin films through GLAD enables to develop advanced materials and devices with unique morphologies aiming to high-performance technological applications [10,11], with tailored functionalities [12,13].

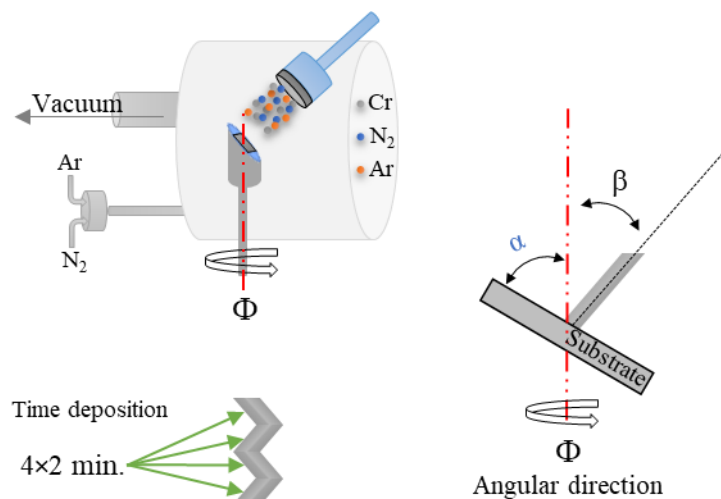


Figure 1: Schematic diagram of the Oblique Angle Deposition set-up. α is the applied angle of the substrate relative to the Cr particle flux, β is the column growth angle, and Φ is the angular direction.

1.1. Thin films based on chromium

Coatings based on transition nitride materials have received a great technological attention in the field of the cutting tools or components subjected to wear and corrosion as they provide high protections to the materials on which they are coated [14,15]. Among various nitrides, and to explore the possibility of developing hard coatings with sensing capabilities, chromium nitride (CrN_x) is among the most interesting ones based on its good mechanical properties [16], corrosion resistance [17], excellent wear behavior [18], electrical conductivity [19] and is widely used in bearings, machine parts and polymer injection molds [6]. To extend the range of applications of the CrN_x materials, and to turn possible the implementation of coatings with multifunctional capabilities, it has been increasingly recognized that hard coating materials with sensing capabilities are needed [6,20–23] being temperature the most relevant parameter to be monitored in a variety of applications and processes [24]. Additionally, among the various chromium oxides, Cr_2O_3 is the most stable under ambient conditions, and it is characterized by its chemical inertness, stability, mechanical strength and relatively high hardness [25]. Previous research shows that the hardness of chromium oxide coatings strongly depends on the stoichiometric

polycrystalline Cr_2O_3 phase present in the coating [26–29], with high-quality Cr_2O_3 stoichiometric coatings reaching nearly 30 GPa combined with good scratch resistance. As chromium oxide is an insulating antiferromagnetic material it is also suitable as a tunnel junction barrier [30]. Depending on its stoichiometry CrN_x shows a metallic-like ($\rho_{\text{CrN}} \approx 6.4 \times 10^{-4} \, \Omega \, \text{cm}$) or semiconducting behaviour ($\rho_{\text{CrN}} > 1 \times 10^{-2} \, \Omega \, \text{cm}$) [31] while chromium oxide is a wide-bandgap semiconductor ($E_g \approx 4 \, \text{eV}$) [32–34]. Combining both nitrogen and oxygen (oxynitride) opens the possibility to tune the energy bandgap and hence the electronic properties in a wide range.

In this scope, it is to notice that few studies report on the relation between the relative humidity and temperature sensibility of chromium oxynitride (CrN_xO_y), the deposition process and the possible morphologies to obtain relative humidity sensors. CrN_xO_y is an interesting material system since it can combine the properties of chromium nitride and chromium oxide, being harder than CrN [35,36] and corrosion resistant like Cr_2O_3 [37]. Moreover, it is to notice that a nanostructured material with high porosity and large surface area will facilitate the adsorption of water vapor on its surface giving great scope for enhancement in the sensitivity of a relative humidity sensor.

1.2. Main goal of the work

Thus, the present work focuses on the investigation of the relationship between the: i) the thermoresistive response of the CrN_x thin films and ii) the relative humidity response of the CrN_xO_y thin films prepared under different processing conditions. The variation of the film's geometry and deposition parameters allows to modify not just the structural properties of the Cr-based thin films, but also, the thermoresistive properties and the relative humidity response, leading to interesting multifunctional characteristics for a variety of technological applications [21–23].

1.3. Thesis structure

This thesis is divided into 6 different chapters: Introduction, State-of-the-Art, Materials and Methods, Results and discussion, Conclusion, and finally Future work.

This thesis addresses two separate types of transducers based on CrN_x and CrN_xO_y thin films to be used as temperature and humidity sensors. Because of that, we chose to present the results and discussion divided into two subchapters: temperature sensors and relative humidity sensors.

The first chapter, “Introduction”, aims to present the problem which we, in some way, pretend to contribute to solve, the main goal and the thesis structure.

The second chapter, “State-of-the-art”, aims to give the reader a general knowledge about temperature sensors and relative humidity sensors, the sensors that are available in the market and some of the sensors that were already made or explored.

The third chapter is devoted to the experimental details. The basic principles of the technique selected for the thin film’s preparation are explored, in a first stage. Then, an introduction of the methods used to produce and characterize the samples and a presentation of the conditions in which these methods were performed are given.

The fourth chapter is assigned to the results of the characterization introduced in the third chapter and the discussion of these results. In this chapter, the chemical, structural, morphological, electrical, thermoresistive and humiresistives properties are analysed.

The fifth chapter states the conclusions achieved by the reported characterization and evaluates the quality of the achieved sensors.

The sixth chapter aims to present future steps to increase the knowledge about this area of work and to increase the functionality of these sensors.

2. State-of-the-Art

This chapter aims to give to the reader the state-of-the-art on sensors to measure relative humidity and temperature. The chapter is divided into 2 subchapters: one on temperature sensors and the other on relative humidity sensors.

2.1. Temperature sensors

In terms of temperature control, temperature is one of the most important factors to human comfort, development and survival. Since the first device, developed by Galileo Galilei in the year of 1592 [38], there has been an increasing evolution to control the temperature measurements [39] due to the fact that temperature control is a critical aspect in several processes such as chemical reactions [40,41], energy measurement [41], combustion [40], extrusion processes [40], separation [40] and storage. Nowadays there is a wide range of sensors to be used in industry control such as thermocouples [42], resistance temperature detectors (RTDs) [42], thermistors [42], infrared pyrometers [42], diode temperature sensors [42], bi-metallic thermometers [42] and liquid thermometers [42], among others [42,43]. Independently of the application, for the industry, the most commonly used temperature sensors are thermocouples and RTDs making around 99% of temperature sensors in use [40]. The transduction mode of the thermocouples is based on the Seebeck effect and are made with two metals of different electrical conductivities [39,44]. When a temperature gradient is applied over the metal, electrons will migrate from the hotter region to the colder region producing a voltage between both regions. The difference between the voltage measured will be proportional to the temperature gradient [39,44]. The most common thermocouples reported are based on SiC-SiC, W-CNi, PtRh-Pt, C-C, C-W, W-Mo, and SiC-C [44,45]. The RTDs are made from one metallic element material such as platinum, copper or nickel [39,44]. Metallic materials possess a positive resistive variation with temperature due to the increase in vibrations amplitude of the metal atoms which will decrease the electrons mobility [44]. The metal most used in RTDs is platinum since it is resistant to high temperatures, is chemically inert and the electrical response are practically linear with the temperature [39,44].

Another attractive temperature sensors are the thermistors [44]. Thermistors are commonly made by semiconductors materials such as metal oxides and may have a positive resistance variation with temperature, called PTC (positive temperature coefficient) thermistors, or have a negative resistance variation, called NTC (negative temperature coefficient) thermistors [44]. Between this two, the most appealing thermistors are the NTC thermistors since they possess a much larger sensibility than both RTDs and thermocouples. Additionally,

they are also smaller and have a higher electrical resistance than RTDs making it less affected by the problems associated with the connection between the RTD and the wires [44]. The principal characteristics of the available commercial temperature sensors are presented in Table 1.

Table 1: Characteristics of the most widely applied temperature sensors, platinum RTDs, thermocouples and thermistors, adapted from [40].

Quality	RTD	Thermocouple	Thermistor
Sensitivity	0.001 K	0.05 K	0.0001 K
Minimum size	2 mm	0.4 mm	0.4 mm
Repeatability	0.02K – 0.5K	1K – 8K	0.1K – 1K
Temperature range	73K – 1123K	73K – 2273K	173K – 573K
Drift	0.01K – 0.1K	1K – 20K	0.01K – 0.1K
Signal output	1V – 6V	0V – 0.06V	1V – 3V

Thermistors are widespread in the market with a great variety of shapes and sizes [43,46] as demonstrated in Fig. 2. However, thermistors have some weakness related to the corrosion, wear and oxidation [43,46,47]. To reduce these drawbacks, they need to be encapsulated to have a good chemical, physical and electrical stability. Yet, one of the advantages of the thermistors and also the RTDs is the fact that they can be produced into the form of thin film increasing the functionality and the wide range of applications. If the metal-based material used has good properties to chemical, physical and electrical properties, they could be a good choice to implement as a sensor in several harsh applications.



Figure 2: Some thermistors shapes and sizes [43].

2.2. Relative humidity sensors

Water vapor is a natural component of air, and it plays an important role in a wide range of practical measurement situations [48,49]. Hygrometry, measurement of water vapor content of a gaseous atmosphere, is in fact a “branch of applied physics in which the multitude of techniques is an indication of complexity of the problem, and of the fact that no one solution will meet all requirements at all times and in all places” [50]. Currently, humidity sensors have been used intensively in several areas such as medicine, agriculture, meteorology, cuisine, storage, civil engineering and naturally in industry processes [4,51]. The need to control humidity has been promoting a continuing development of new and improved humidity sensors to enhance the selectivity, sensibility and stability, while also striving to decrease the response time, the size and the price of the sensors [51]. Humidity sensors can be separated into five categories: optical, electrochemical, electrical, thermometric, and mass sensitive sensors [4]. From these, electrical humidity sensors, particularly capacitive and resistive humidity sensors, have received a great deal of attention due to their properties. Table 2 shows the advantages and disadvantages of capacitive vs resistive humidity sensors. Apart from these two, there is also thin film and field-effect transistors, hetero junction-based humidity sensors and Kelvin probe humidity sensors [52].

Table 2: Capacitive and resistive humidity sensors comparison [52].

Humidity sensor type	Advantages	Disadvantages
Resistive humidity sensors	Easier to use, cheap, small, mass reproducible, high sensitivity,	Non-linear, limited range, poor stability, drift, high-temperature dependence,
Capacitive humidity sensors	Low maintenance, cheap, small, mass reproducible, tolerate condensation, fast response, linearity, broad humidity range	Loses accuracy at low humidity, high humidity and high temperature, need for electronics, drift

However, there are a wide variety of resistive humidity sensors as reported in [4,48,52]. For both capacitance and resistive humidity sensors, ceramics have been widely explored due to their promising results such as their high mechanical strength, high corrosion resistance and thermal stability [53,54]. Table 3 shows the advantages and disadvantages of each material base used as a humidity sensor.

Table 3: Advantages and disadvantages of resistive humidity sensors made from different materials [4,48,52]

Material	Advantages	Disadvantages	References
Polymer	Low cost, small, no calibration needed, long life, fast response, high accuracy, broad range, and excellent reproducibility	Chemical contamination may cause failure, temperature dependency	[55–58]
Metal Oxides	High sensitivity, low cost, fast response, broad range, high mechanical strength, high thermal capability, physical stability and high corrosion resistance, high versatility	Need for periodic cleaning, drift, temperature dependency, hysteresis, contamination	See Table 3
Black phosphorus	Ultra-sensitive, short response time, broad range	Short-term stability, low repeatability, temperature dependency	[59–62]
Carbon-based sensors	Flexible, elastic, high hardness, broad range, may have fast response and recovery	Temperature dependency, high hysteresis, may have a slow response and recovery times	[63–67]
Chalcogenides	Fermi-level at the surface can be changed, very fast response	Low selectivity, drifts at high temperatures	[68–72]

Like temperature sensors, thin films for relative humidity sensors have the advantage of improving the functionality of the component surface with a very reduced size and cost. Chromium oxide, Cr_2O_3 , is a very hard coating and has high corrosion, oxidation, and wear resistance. In this sense, Cr_2O_3 is a perfect candidate to be used in humidity sensor applications. Chromium-oxide based materials such as MgCr_2O_4 [73], ZnOCr_2O_4 [74], $\text{PANI-Cr}_2\text{O}_3$ [75], $\text{PPy-Cr}_2\text{O}_3(\text{PCO})$ [76], $\text{Cr}_2\text{O}_3\text{-WO}_3$ [77] have also already been proved to be an excellent alternative to the commercial humidity sensors. Table 4 summarize the commonly used materials to produce resistive humidity sensors.

Table 4: Metal oxides used on resistive humidity sensors adapted from [4]

Type of oxides	Oxides
Binary oxides	CeO ₂ [78]; SnO ₂ [79]; CuO [80]; ZnO [81–83]; WO ₂ [84,85]; TiO ₂ [86–92]; VO ₂ [93]; V ₂ O ₅ [94]; MnO ₂ [95]; Mn ₂ O ₃ [95]; Mn ₃ O ₄ [95]
Mixed oxides, complex oxides, and composites	Sr _{0.95} La _{0.05} SnO ₃ [96]; MnWO ₄ [97,98]; Ba _{0.99} La _{0.01} SnO ₃ [99]; MgO-Al ₂ O ₃ [100]; MnO-ZnO-Fe ₂ O ₃ [101]; Zn _{1-x} Co _x MoO ₄ [96]; SnO ₂ :MgO [102]; PbWO ₄ [103]; La ₂ O ₃ -TiO ₂ -V ₂ O ₅ [104]; Fe ₂ O ₃ /SiO ₂ [105]; ZnMoO ₄ -ZnO [106]; La ₂ CuO ₄ [107], MgCr ₂ O ₄ [73], ZnOCr ₂ O ₄ -LiZnVO ₄ [74], Cr ₂ O ₃ -WO ₃ [77]
Perovskites and Perovskites based oxides	BaTiO ₃ [108–114]; CoTiO ₃ [115]; KNbO ₃ [116]; SrTiO ₃ [117]; BaPbTiO ₃ [118]; Ba _{0.5} Sr _{0.5} TiO ₃ [119]; PbSr _x Zr _{0.3} Ti _{0.7} O ₃ [120]; CaCu ₃ Ti ₄ O ₁₂ [121]
Alkali-doped metal oxides	BaTiO ₃ :Na,K [122]; (Mn-Co-Ni-O):Li [123]; Ca _x Pb _{1-x} TiO ₃ :Li [124]; Fe ₂ O ₃ :Li [125]

3. Experimental details

This chapter aims to provide a guided path through the production of Cr-based thin films, designed to enhance temperature and relative humidity sensing. The basic principles of the technique selected for the thin film's preparation are explored, in a first stage. Then, an introduction of the methods used to produce and characterize the samples and a presentation of the conditions in which these methods were performed are given.

3.1. Thin film production

3.1.1. The magnetron sputtering technique

Cr-based thin films were produced by DC (direct current) magnetron sputtering, which is one of the most common processes of Physical Vapor Deposition techniques (PVD). In PVD processes, the particles (atoms or groups of atoms) of the material to be deposited are vaporized by a physical process. Then, the particles are transported from the metallic target, with an aleatory direction, in the form of vapor through a low-pressure gaseous environment (plasma) to the substrate and deposited by condensation, in the form of a thin film [126], Fig. 3. Sputtering is a typical multiple collision process that consists in the ejection of particles from the surface of a solid material due to the momentum exchange with energetic projectile particles impinging in a target, usually, ions of a noble gas - Argon [126]. Then, the sputtered atoms of the target are deposited on some other surface, the process is called sputter deposition.

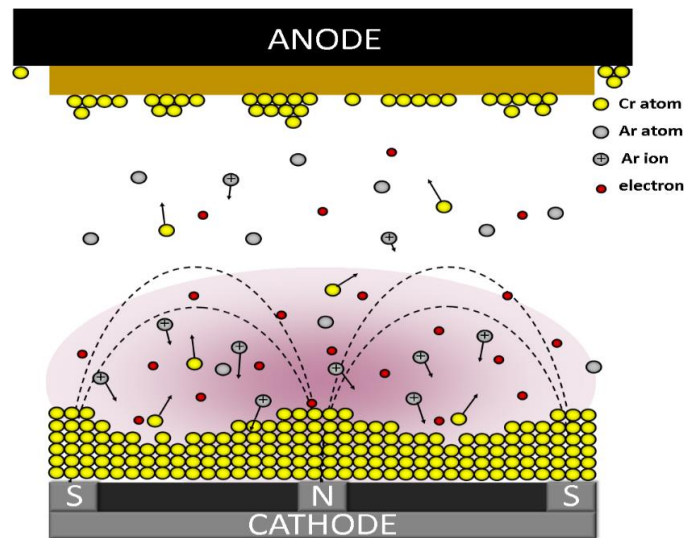


Figure 3: Nuclear processes during the sputtering process.

In the sputter deposition, the vacuum environment is essential to increase the mean free path of the gas molecules and to reduce vapor contamination during processing. The sputtering process begins with the partial ionization of a gas - Argon - at low-pressure by applying a discharge voltage between the electrodes, originating a Plasma. In our work, before the deposition, the chamber is pumped by a turbomolecular pump, Adixen/Alcatel, model ATP 400 (pumping speed of 400 L/s), backed by a primary rotary pump AEG, model AMME 80ZCA4, in order to reach an ultimate pressure lower than 6×10^{-4} Pa, before each deposition. CrN_x thin films were DC-sputtered from a bulk chromium target (20 cm length, 10 cm width and 0,6 cm thickness; 99.96 at% purity) placed at 70 mm from the substrate using a customized vacuum chamber, Fig. 4.

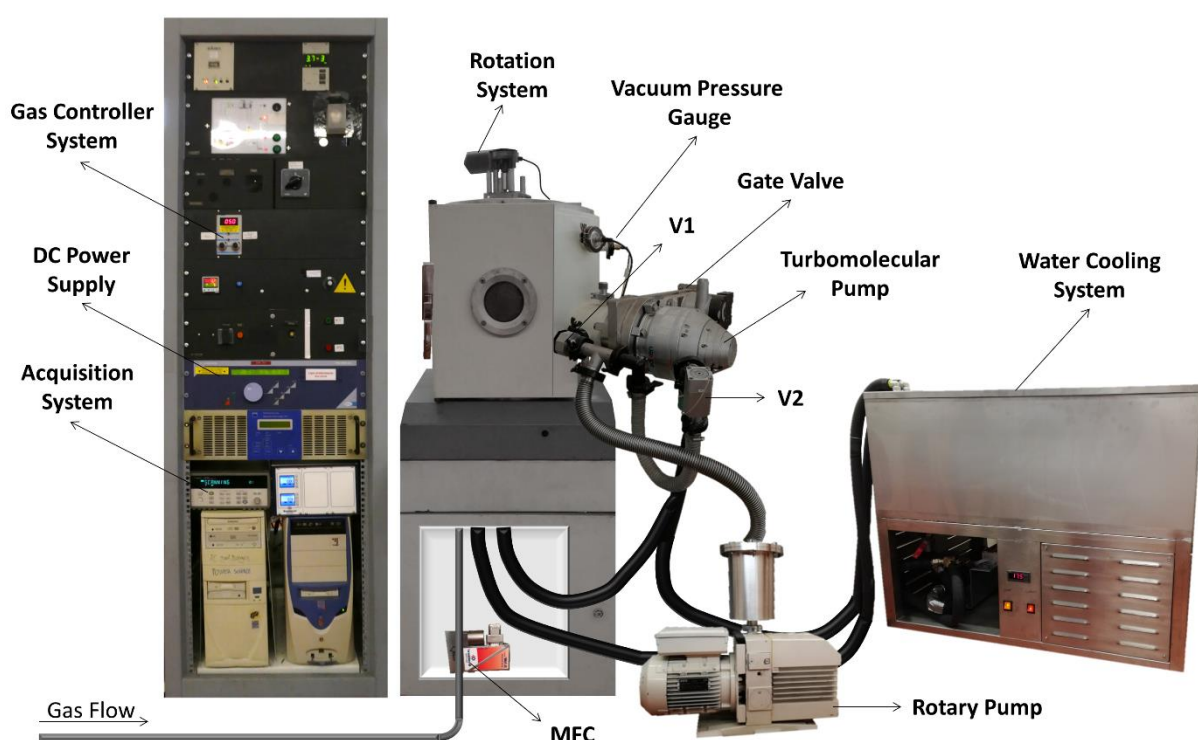


Figure 4: Vacuum chamber used in this work.

3.1.1.1. GLancing Angle Deposition - GLAD

With adequate operating conditions, GLAD technique allows obtaining columnar microstructures with specific architectures by controlling the orientation of the substrate relative to the impinging vapor flux [8], as illustrated in Fig. 5. In the observed columns, when the incident angles of the particles flux α increase with respect to the sample surface, the angle β of the column with respect to the sample surface, increases the same way [8]. In this work, the intended morphology is the zigzag columnar growth. This growth is achieved by changing

periodically (rotated in the Φ direction) the angle of incidence from 60° to -60° and vice versa during the deposition process. The deposition is separated in 4 cycles as demonstrated in Figure 4.

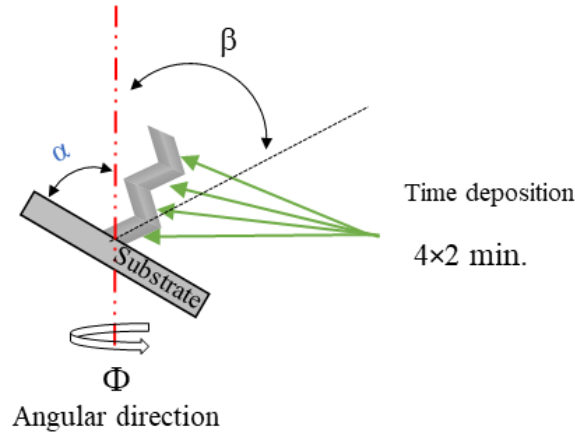


Figure 5: Schematic diagram of the GLAD Deposition set-up. α is the applied angle of the substrate relative to the Cr particle flux, β is the column growth angle, and Φ is the angular direction.

3.1.1.2. Deposition conditions

Cr-based thin films were sputtered at room temperature. Before all depositions, the samples (glass ISO norm 8037–1 microscope slides and (100) p-type silicon wafers) were placed in a reactor from Diener electronic, model Zepto, to clean the substrates using a pure Argon atmosphere at a RF power of 100 W during 900 s. Then the Cr-based thin films were deposited according to the table 5. For that, a constant Argon flow rate of 25 sccm was applied and the work gas atmosphere was composed of Argon and reactive N_2 or mixture of N_2 - O_2 gas (85/15). The maximum voltage was limited at 400 V as well as the current intensity at 1 A. All depositions were done for 8 min., two minutes each chevron as demonstrated in Fig. 5.

In order to obtain a stable electrical response, an annealing protocol was carried out after all depositions. The protocol involves an in-air annealing process of the films from room temperature to a maximum temperature of 523 K, with a constant rate of 10 K min^{-1} . This maximum temperature was then held for 120 min, followed by a cooling stage at a constant rate of 10 K min^{-1} to room temperature.

Table 5: Varying conditions of the depositions

Reactive gas	Reactive gas flux (sccm)	Voltage (V)	Base pressure ($\times 10^{-6}$ mbar)	Work pressure ($\times 10^{-3}$ mbar)
None	0	290	6,9	2,6
N ₂	2	286	6,6	4,1
N ₂	4	286	8,0	4,1
N ₂	6	288	6,6	4,2
N ₂	8	291	7,4	4,2
None	0	290	6,9	2,6
N ₂ +O ₂	2	286	6,6	4,1
N ₂ +O ₂	4	286	8,0	4,1
N ₂ +O ₂	6	288	6,6	4,2
N ₂ +O ₂	8	291	7,4	4,2
N ₂ +O ₂	10	305	9,6	4,2

3.1.2. Morphological, composition and structural characterization

3.1.2.1. Scanning electron microscopy – SEM

The morphological properties of the Cr-based thin films were evaluated by scanning electron microscopy (SEM). This technique permits to acquire surface and cross-section imaging of the samples, with high resolution, that enable the characterization of the microstructure, the determination of the sample thickness, and the identification of defects, impurities and porosity [127]. This technique is based on the incidence of electron beam focused on a nanometric area of the substrate surface, with energies between 2 keV and 50 keV, using the backscattered electrons and secondary electrons to obtain images with a resolution of just a few nanometers.

The top view and fractured cross-section of the Cr-based thin films were characterized using a NanoSEM–FEI Nova 200 (FEG/SEM) microscope (Center for Electron Nanoscopy, Lyngby, Denmark). At the same time, the composition of the CrN_x samples was obtained by Energy Dispersive X-ray Spectroscopy (EDS) with an EDAX - Pegasus X4M (EDS/EBSD). The SEM apparatus is normally equipped with an EDS instrumentation which permits in a simple way to quantify the elemental composition of the samples produced [128]. It relies on the interaction of some source of X-ray excitation and a sample. The X-ray beam is directed into a sample and the photons emitted by the sample atoms are detected. The incident photons interact with the atoms and may cause the ionization of the lower orbits of the electron-cloud, this will create an electron-hole and since particles tend to their ground-state, an electron from a higher orbit transitions to a lower orbit to occupy the hole this transition emits characteristic radiation and its measurement enables the sample composition evaluation [129].

3.1.2.2. Rutherford Backscattering Spectrometry

The composition of the CrN_xO_y samples was obtained by Rutherford backscattering spectrometry (RBS).

Rutherford backscattering spectrometry (RBS) allows quantitative compositional analysis without the use of reference standards [130]. For analysis, high-energy He^{2+} ions are directed onto the sample and the yield of the backscattered He^{2+} ions at a given angle is measured (Figure 5). Because the backscattering cross section for each element is known, it is possible to obtain a quantitative compositional depth profile from the RBS spectrum [130]. RBS has the following advantages: quantitative and non-destructive surface analysis, no need for reference standards, measures the composition and thickness of nanoparticles, measures mass and depth of the target sample, can determine the ratio of one element to another, and can determine the lattice location of impurities in single crystals [130].

The ratio between the final kinetic energy, E_f , and the initial kinetic energy, E_i , is determined by [131]:

$$\frac{E_f}{E_i} = \left(\frac{r \cdot \cos \theta_1 + \sqrt{1 - r^2 \cdot \sin^2 \theta}}{1 + r} \right)^2, \quad (3)$$

where θ_1 is the scattering angle, and r is the ratio between the alpha particle mass, m_1 , and the sample particle mass, m_2 [131].

$$r = \frac{m_1}{m_2}, \quad (4)$$

These equations allow the calculation of the sample atoms mass, m_2 , and by that, the determination of the sample composition [131].

In our work, RBS measurements were made in the small chamber where three detectors were installed: standard at 140° , and two pin-diode detectors located symmetrically to each other, both at 165° . Spectra were collected for 2 MeV $^4\text{He}^+$ and also at 2.3 MeV $^1\text{H}^+$. The angle of incidence was 0° (normal incidence). The RBS data were analysed with the IBA DataFurnace NDF v10.0a [130], the double scattering was calculated with the algorithms given in [132], and the pileup handling was calculated with the algorithms given in [133].

3.1.2.3. X-ray diffraction measurements

The structure of the films was characterized by X-ray diffraction (XRD). This technique is used to evaluate the structure, crystallite size, crystallite deformation and crystallite growth preferential orientation. The X-ray diffraction apparatus is composed of 3 components: The X-ray source, the sample holder and the x-ray detector. The X-ray source and the detector will move in relation to the sample holder at the same speed maintaining the same angle with the sample holder (fig. 6).

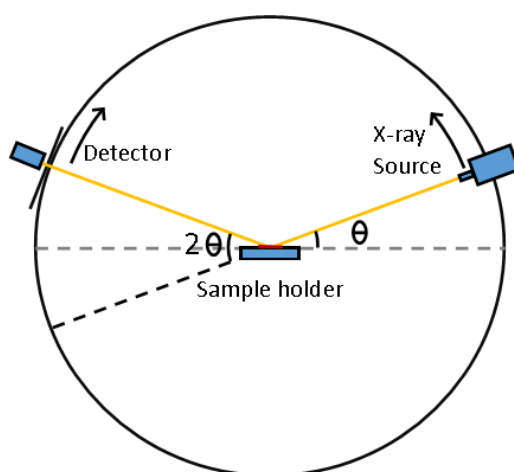


Figure 6: XRD schematization, the detector and X-ray source move by $-\theta$ and by θ providing the 2θ measurement.

The interplanar distance of the sample was calculated by the Bragg Law [134]:

$$2d \cdot \sin(\theta) = n \cdot \lambda, \quad (6)$$

where d is the interplanar distance of the sample, θ is the angle obtained by the crystallography, λ is the wavelength of the radiation source and n is a positive integer [134]. This equation may be understood as the left side of the equation being the path-length difference (figure 7 b)) and the right side of the equation as the path length needed in order to make constructive interference happen, in other words, a multiple of the wavelength (fig 7).

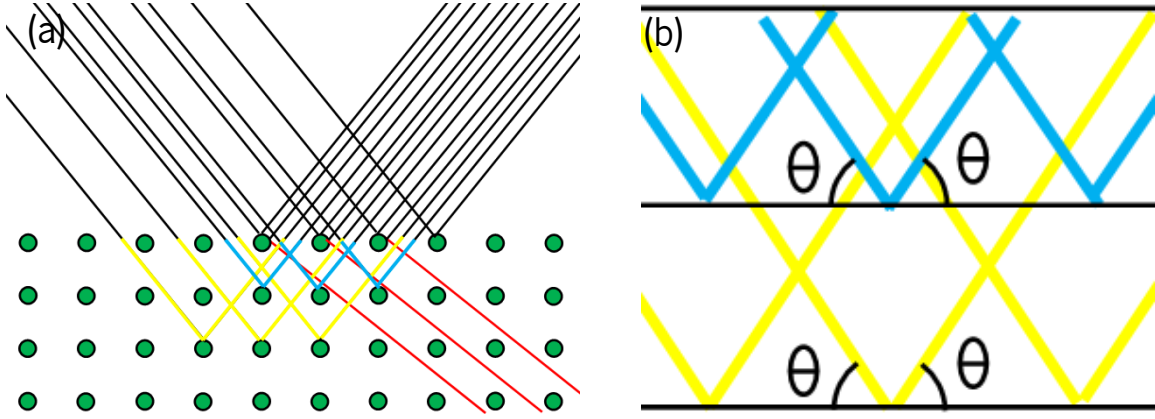


Figure 7: Bragg law a) X-rays diffracting on the sample atoms, b) path-length difference.

By the relation for the cubic structure, the lattice constant, a , is calculated through [134]:

$$d^2 = \frac{a^2}{h^2 + k^2 + l^2}, \quad (7)$$

where h , k and l are the Miller indices [134].

The grain size was calculated by the Scherrer formula [134]

$$\tau = \frac{K \cdot \lambda}{\beta \cdot \cos(\theta)}, \quad (8)$$

where τ is the grain diameter, K is the shape factor, which is considered to be 0.9 since spherical crystallites are assumed, β is the full width at half maximum (FWHM) in radians [134].

In order to quantify the preferential crystallite orientation, i.e., the preferred growth texture of a particular plane, the texture coefficient $Tc_{(hkl)}$ was calculated after Eq. 9 [135]:

$$Tc_{(hkl)} = \frac{I_{(hkl)}/Ir_{(hkl)}}{\frac{1}{N} \sum_{k=0}^n I_{(hkl)}/Ir_{(hkl)}}, \quad (9)$$

where $I_{(hkl)}$ is the intensity of a particular reflection, $Ir_{(hkl)}$ is the intensity of the reference peak obtained from the database (ICSD), and N is the total number of reflections considered in the obtained diffractogram.

In our study, the structure of the films was characterized by an XRD apparatus using a Bruker D8 Discover diffractometer (Bruker, Billerica, Massachusetts, EUA), operating in a θ - 2θ configuration and a step of 0.02° per 0.2 s from 30 to 75° ($\text{Cu } \lambda_{\alpha 1} = 1.54060 \text{ \AA}$).

3.1.3. Electrical, thermoresistive and relative humidity measurements

3.1.3.1. Electrical resistive measurements

The electrical resistivity of the samples was measured by a Four-Point Probe System (Ossila Ltd, Solpro Business Park Windsor Street, Sheffield, UK). The probe head uses spring-loaded contacts instead of sharp needles, with 1.27 mm spacing between the probes, 0.48 mm probe diameter, and 60 g spring pressure.

3.1.3.2. Thermoresistive measurements

The thermoresistive properties were obtained from the electrical resistance vs temperature measurements with the setup presented in Figure 8. For that, the electrical resistivity of the samples was measured in two cycles over the range of 305 K to 473 K, regulated with a Linkam's LTS420 stage at a rate of 10 K min^{-1} and the electrical resistivity measured with a multimeter Keithley serie 2700.

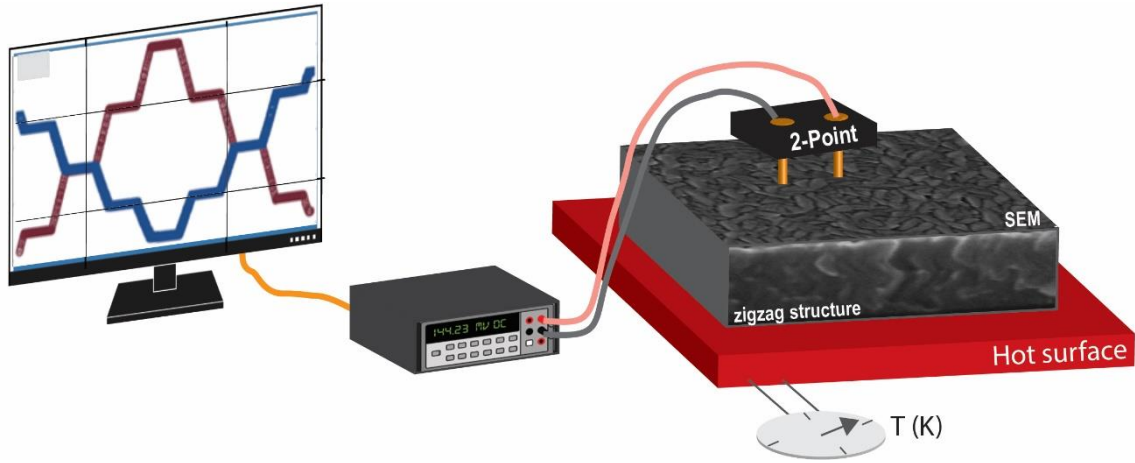


Figure 8: Schematic representation of the thermoresistive setup.

Commonly, the electrical resistance of a material varies with temperature because temperature affects the number of carriers in semiconductors or their mobility in conducting materials. In some materials, the electrical resistance will decrease with increasing temperature, due to the charge carriers excitation by thermal energy, while for others the electrical resistivity will increase as mobility of the carriers will decrease with increasing temperature due to the scattering effect of lattice vibrations. Thus, when the temperature increases, the resistivity of the semiconductors may decrease (negative temperature coefficient of resistance - NTCR) or increase (positive temperature coefficient of resistance - PTCR), depending upon the change in the number of carriers and their mobility.

For semiconductor temperature sensors, the temperature dependence of electrical resistance is generally represented in the following form [136]:

$$R_T = A \cdot \exp\left(\frac{\beta_G}{\Delta T}\right) \quad (10)$$

where R_T is the electrical resistance at temperature T (K), A (Ω) and β_G (K) is the thermal indexes, which are used to evaluate the sensitivity of the thermo-resistive effect in thermistors, and T (K) is the absolute temperature. The relationship between β_G and TCR can be written as [136]:

$$TCR = \frac{\Delta R}{R_0} \cdot \frac{1}{\Delta T} = \frac{\beta_G}{T^2} \quad (11)$$

In Equation 11, ΔR (Ω) is the variation of the film's resistance, R_0 (Ω) is the initial resistance of the film at 25 °C (room temperature) and ΔT (K) is the variation of temperature. Equations 10 and 11 are only valid over small temperature ranges, where the slope of the $\ln(R_T)$ versus $1/T^2$ approximates to a linear relationship [6].

3.1.3.3. Relative humidity measurements

The relative humidity measurements were done using a homemade setup using a hermetic vapor chamber (P-Selecta) with temperature control as described in [137] and represented in Fig. 9.



Figure 9: Schematic representation of the humidity chamber setup using a hermetic vapor chamber (P-Selecta) with temperature control.

The humidity was created by an ultrasonic humidifier beaker with distilled water. The sensors were placed in the humidity chamber along with a commercial temperature and relative humidity datalogger (Amprobe TR200-A). The temperature within the test chamber was kept at 24 °C during the experiments. The variation of the electrical resistance of the developed sensors was measured using an HP 34401 digital multimeter connected to a PC for data acquisition. The resistance of the sensors was obtained for a relative humidity variation from approximately 40% to 90% with an accuracy of $\pm 5\%$ RH.

The relative humidity dependence with the electrical resistance is generally represented in the following form [138]:

$$SR = \frac{S}{R_0} = \frac{\Delta R}{R_0} \times \frac{1}{\Delta RH}, \quad (12)$$

where SR is the sensor response, ΔR is the resistance variation, R_0 is the resistance at room temperature and ΔRH is the relative humidity variation.

4. Results and discussion

In this chapter we present the results obtained for the two systems. First, the chapter presents the work focuses on the investigation of the relationship between the microstructure and the thermoresistive response of CrN_x. Then, the relationship between the microstructure and the relative humidity sensing response of CrN_xO_y thin films under distinct amounts of nitrogen (N₂+O₂) in a mixture relation of 85% N₂ and 15% O₂, both deposited by DC-reactive magnetron sputtering.

4.1. Temperature sensor results

4.1.1. Structural and Morphological Characterization

The crystal structure and texture evolution of the CrN_x thin films have been evaluated by XRD, and the obtained diagrams are presented in Fig. 10, which shows the phase evolution of the CrN_x thin films deposited onto Si substrates.

The XRD diagrams (Fig. 10) suggest that the CrN_x thin films are characterized by a polycrystalline structure. In general, with the increase of the N₂ flux, it is observed an increase of the CrN_x (111) (ICSD card no. 00–900–8619) peak intensity [139]. The observed changes in the peak intensities and full width at half maximum (FWHM) as N₂ flow rate vary from 0 up to 8 sccm can be attributed to differences in N₂ content in the CrN_x, as reported in Tab. 6 and verified in [139]. This feature indicates a clear transition from a Cr-type with base-centered cubic, BCC, structure and space group Im-3m (ICSD card no. 00 – 001–1261) to a CrN-type with face-centered cubic, FCC, structure and space group Fm-3m (ICSD card no. 00–900–8619). At N₂ flow rates of 2 and 4 sccm, a coexistence of FCC cubic (ICSD card no. 00–900–8619) and hexagonal (ICSD card no. 00–003–1191) phases associated with CrN-type, is observed: while at N₂ flow rate of 4 the shoulder at the right of the CrN (111) peak can be attributed to hexagonal Cr₂N (110) (ICSD card no. 00–003–1191), the peak situated at $2\theta \approx 45^\circ$ can be a reminiscence of the Cr BCC phase.

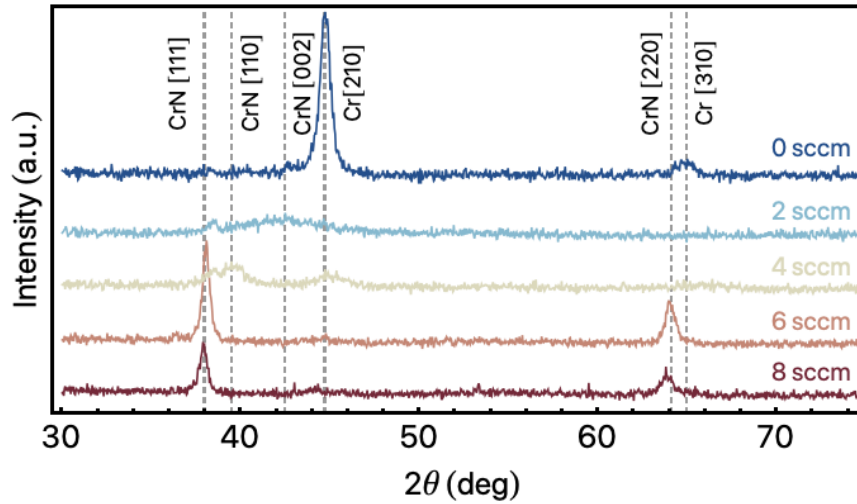


Figure 10: X-ray diffraction diagrams for the Cr and CrN samples. The peaks are indexed by using the ICSD card nos. 00–900–8619 and 00–003–1191 for CrN and Cr₂N, respectively.

Additionally, EDS measurements allow to identify a low concentration of O₂ in the samples which is expected due to some superficial contamination, as well as from the annealing protocol, but not confirmed in the XRD diffractograms, in terms of any oxygen containing crystalline phase. The atomic percentages of Cr are reduced with increasing N₂ content, while oxygen contents are enhanced during the annealing protocol, Tab. 6, indicating the occurrence of surface oxidation around the coatings as the temperature increases up to 523 K. However, we observe the absence of the peaks located at 41.4° (113) and 51.3° (024), associated with Cr₂O₃ phase (ICSD card no. 00 – 38 – 1479). The formation of Cr₂O₃ during annealing in air has been discussed in [140] and, from the results, the formation of Cr₂O₃ phase needs an air-annealing temperature higher than 873 K. The samples could also include an amorphous phase, but it has not been observed within the detecting precision of the XRD.

Table 6: Elemental composition of the CrN samples.

N₂ Flow rate (sccm)	[Cr] (±5 at%)	[N] (±5 at%)	[O] (±5 at%)
0	96.5	0.0	3.5
2	59.0	34.9	6.2
4	49.9	42.6	7.5
6	46.5	45.5	8.0
8	47.1	45.0	7.9

The texture coefficient calculated for the highly oriented peaks is represented in Fig. 11 (a). For a sample with randomly oriented crystallites $Tc_{(hkl)} = 1$, while higher values indicate the abundance of grains oriented along the (hkl) direction. Fig. 11 (a) shows that the highest $Tc_{(hkl)}$ value has been found for CrN. samples growth with an N_2 flux of 6 sccm ($Tc_{(111)} = 1.934$) and 8 sccm ($Tc_{(111)} = 1.430$). On the other hand, for CrN. samples growth with an N_2 flux of 2 and 4 sccm, the texture coefficient shows a value near the unity, Fig. 11 (b) ($Tc_{(111)} = 1.032$) and ($Tc_{(111)} = 0.960$) respectively, which is related to the coexistence of the cubic and hexagonal phases. Additionally, in order to determine the crystalline size (D_s) of the studied films, the Debye–Scherrer method [141] was used (Figure 11 (c)), demonstrating that increasing N_2 flux leads to a crystallite size increase from ≈ 20 nm up to ≈ 23 nm.

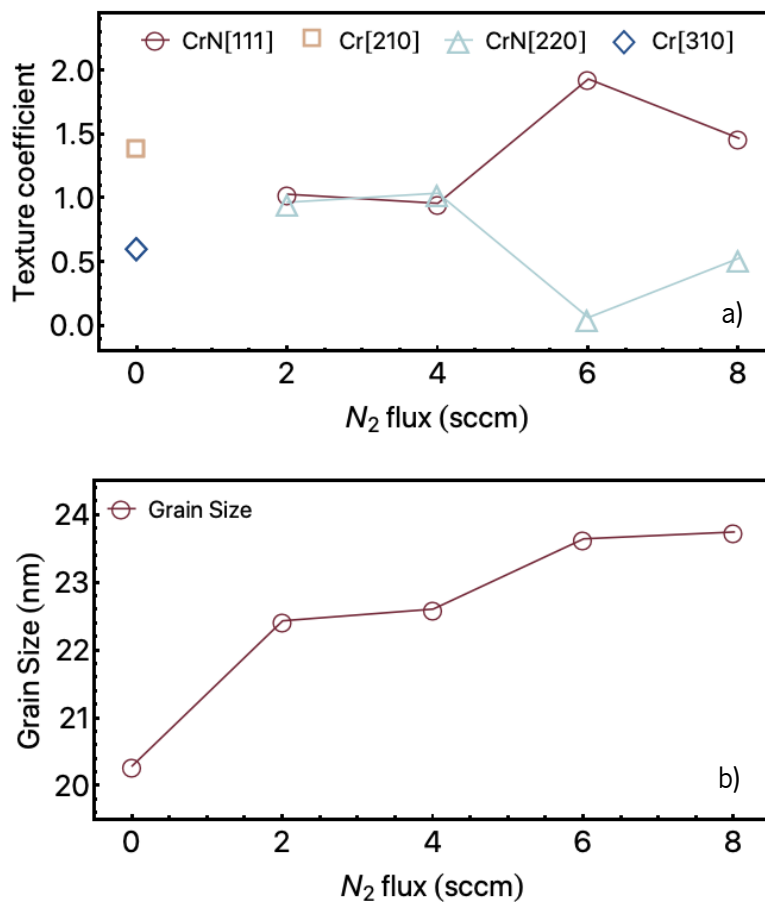


Figure 11: (a) Texture coefficient $Tc_{(hkl)}$ variations of the CrN thin films at different N_2 concentrations. (b) Grains size of the films as a function of N_2 concentrations obtained from the XRD results.

SEM micrograph images for the different films are represented in Fig. 12. Showing the characteristic zigzag columns of the Cr and CrN_x thin films. Increasing N₂ flux leads to a variation of the morphological features, namely in the columnar arrangement (type, density, and surface aspect). For the Cr samples (Fig. 12 (b)), the shape of the column looks like an elliptical profile and some porosity alignment is observed. By increasing the N₂ flux up to 8 sccm, the zigzag-like structure is maintained. On the other hand, from the top view micrographs for the sample with an N₂ flux of 4 sccm, Fig. 12 (c), it is observed that the surface of the films seems to grow without a preferential alignment, as also indicated by XRD results and confirmed by a texture value near the unity. Increasing, the N₂ flux to 8 sccm (Fig. 12 (d)) leads to a reduction of the definition of the zig-zag columns when compared with the Cr samples, but the porosity increase between columns and columnar gaps are easily detected on the surface of the films.

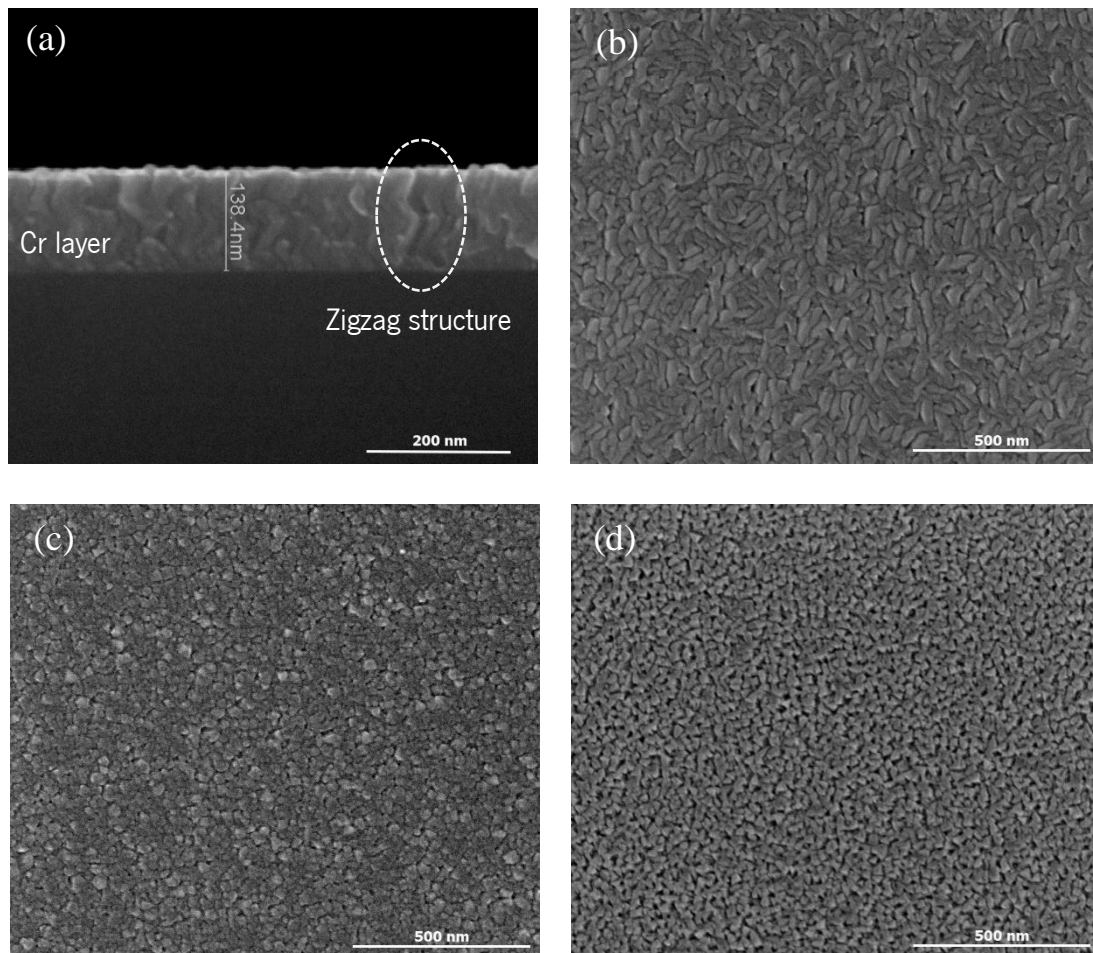


Figure 12: Representative SEM micrographs of the Cr samples, (a) Cr cross section, (b),(c) and (d) top view of the Cr, CrN-4sccm, and CrN-8sccm samples, respectively.

However, the results of the crystallite size (D_s) of the films, calculated by the Debye–Scherrer equation, show an increasing trend with the increase of N₂ flux, leading to a maximum average crystallite size near of 23 nm, using

the (111) reflection. In fact, the use of the Scherrer's approach assumes symmetric crystallites and the SEM micrographs show that it is not the case in the studied Cr samples, Fig. 12 (b). Actually, the micrographs show that the CrN_x thin films are formed by short segments of columnar grains for Cr films and that these segments decrease with the increase of the N₂ flux and only the approximate size and not the shape can be inferred using the Scherrer's technique. Therefore, the sizes obtained by using Scherrer's method should be considered only for comparison purposes among samples.

4.1.2. Electrical and thermo-resistive measurements

Temperature-dependent measurements were performed to obtain quantitative information about the sensitivity of the CrN_x thin films and to evaluate their potential as temperature sensing coatings. Before that, and as explained above, the samples were submitted to an annealing protocol at 523 K for 120 min in order to obtain a stable thermosensitive response due to the structural refinement [142].

Figure 13 shows the variation of the electrical resistivity as a function of temperature for the CrN_x thin films prepared with an N₂ flux in the range of 4 up to 8 sccm, Measurements are presented in the temperature range of 300-473 K with a holding step of 600 seconds at temperatures of 323 K, 373 K, 423 K and 473 K to evaluate the stability for the response.

The thermo-resistive response of the samples is very stable for the different N₂ flux conditions in which they were prepared. When the samples prepared with an N₂ flow rate of 4 sccm, Fig. 12 (a) shows a linear response with a hysteresis lower than 0.14%. Increasing the N₂ flow rate from 4 to 6 and 8 sccm, Figs. 12 (c) and (e), leads to a sharp decrease in the linearity and the hysteresis disappears for the sample prepared with 6 sccm, being less than 0.22% for the sample prepared with 8 sccm. Figures 12 (b), (d) and (f) present a magnified time view in the range between 500 s and 2300 s, where it is observed the stability of the electrical signal as a function of temperature and time. The resistance variation rate at a constant temperature of 373 K after 600 s is very low for the CrN_x thin films. Thus, the samples show very good temporal stability at a given temperature as corresponding to a metallic conduction mechanism [143]. Further, the high resistivity and the negative TCR values of CrN_x thin films indicate high scattering caused by a large amount of disorder due to the amorphous structure of the CrN_x thin films [144], the latter not being confirmed by the XRD results.

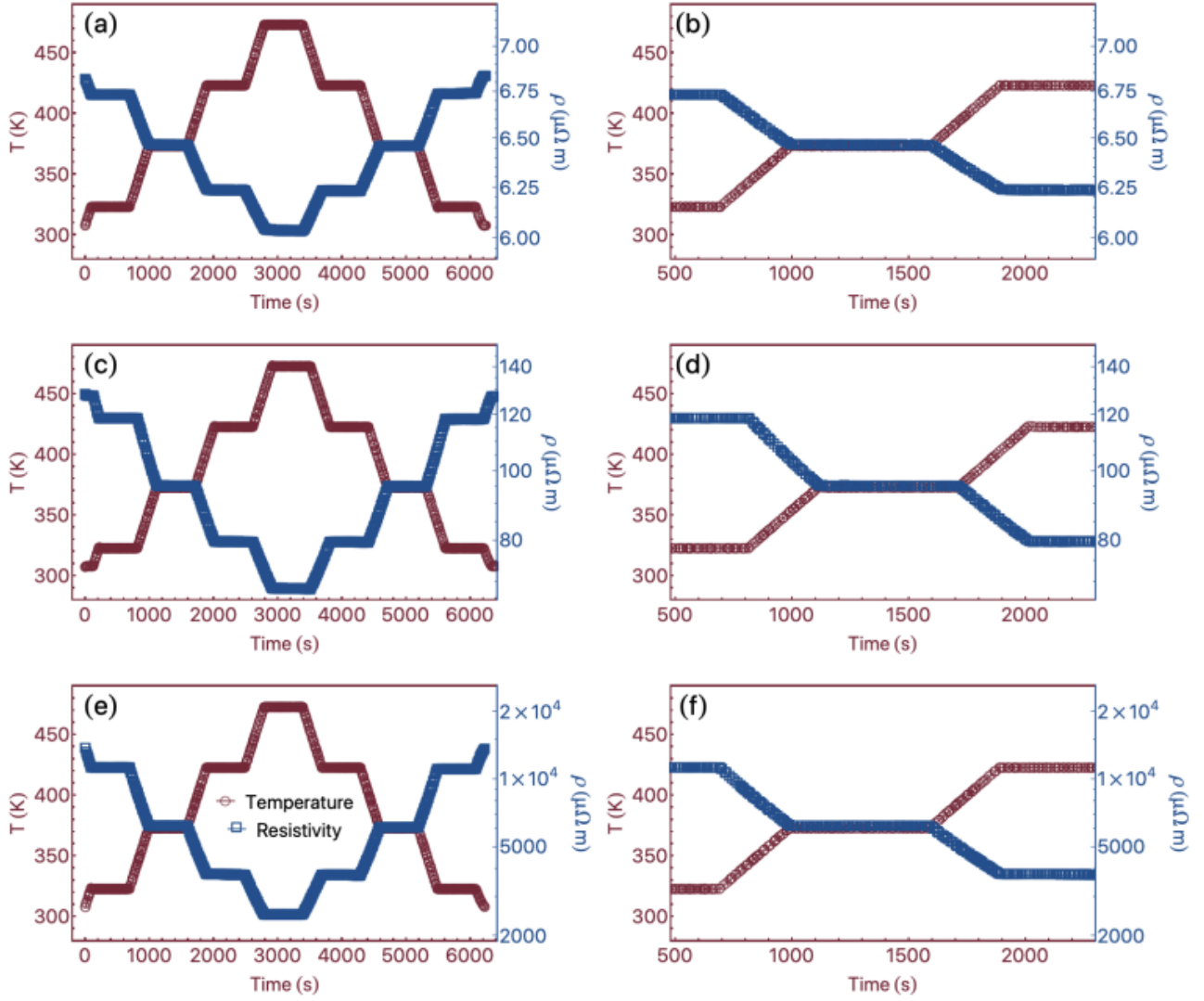


Figure 13: Temperature dependent electrical resistivity over time. (a) Results for the N_2 flux of 4 sccm. (b) Zoomed range of the sample deposited with an N_2 flux of 4 sccm. (c) N_2 flux of 6 sccm. (d) Zoomed curves for N_2 flux of 6 sccm. (e) Results for the samples deposited with N_2 flux of 8 sccm. (f) Zoomed curves for N_2 flux of 8 sccm.

Figure 14 shows the variations of the electrical resistivity and TCR as a function of the N_2 flow rate applied during the reactive sputtering. As the N_2 flow rate increases, the electrical resistivity of the CrN_x thin films increases, which is related to the fact that Cr has been prepared in a metal phase by the reactive sputtering method and it is followed by a nitrification process. In fact, for an N_2 flow rate of 10 sccm, Cr suffered nitrification and became an insulator.

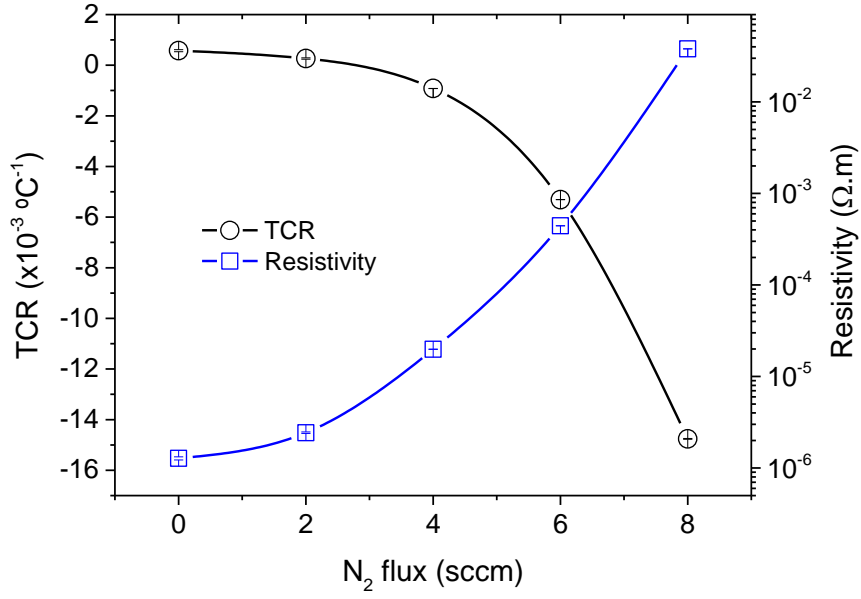


Figure 14: Evolution of the electrical resistivity and temperature coefficient of resistance as a function of the N_2 flux during sample preparation.

The TCR values, according to the procedure applied to the CrN_x thin films, increase with increasing N_2 flow rates. The lowest TCR values are obtained for the lower N_2 flow rates (0 or 2 sccm), the positive TCR is low ($5.74 \times 10^{-4} \pm 3.91 \times 10^{-5} \text{ } ^\circ\text{C}^{-1}$ and $2.65 \times 10^{-4} \pm 2.51 \times 10^{-5} \text{ } ^\circ\text{C}^{-1}$) due to the low resistance, $1.27 \times 10^{-6} \pm 5.02 \times 10^{-8} \text{ } \Omega.m$ and $2.43 \times 10^{-6} \pm 4.54 \times 10^{-8} \text{ } \Omega.m$, respectively, and the electrical resistivity of the Cr thin films almost do not depend on temperature in the measured temperature range. For N_2 flow rates from 4 to 8 sccm, the electrical resistivity increases from $1.98 \times 10^{-5} \pm 5.78 \times 10^{-8} \text{ } \Omega.m$ to $3.80 \times 10^{-2} \pm 6.20 \times 10^{-6} \text{ } \Omega.m$ and negative TCR values of $9.18 \times 10^{-4} \pm 2.47 \times 10^{-6} \text{ } ^\circ\text{C}^{-1}$ to $1.48 \times 10^{-2} \pm 1.74 \times 10^{-5} \text{ } ^\circ\text{C}^{-1}$ were obtained.

A negative TCR can be caused by distinct mechanisms and described by different theoretical approaches. For instance, the weak localization and grain-boundary models are widely used to adjust the experimental results of thin films and nanostructures. In particular, the weak localization model [145] highlights the dependence of the TCR as a function of temperature, considering the electron localization mechanism. This approach has been used to describe both positive and negative TCR systems [146–148]. The Grain-boundary model considers the crystalline structure and the grain-size parameter (D_S) of the samples to describe the electrical resistivity (ρ_S) and the TCR coefficient (β_G) as a function of both, grain-size and temperature. For this reason, this model is widely used for the analysis of thin films, where the D_S parameter can be tailored by changing the deposition parameters.

4.1.3. Grain-boundary model

The model, presented by Mayadas and Shatzkes [149] considers the inner-crystalline mean free path (L) and the mean probability for electrons to pass a single grain-boundary (S). From this model, the electrical resistivity ρ_G can be described by,

$$\rho_G = \frac{\xi}{L} S^{L/D_S}, \quad (13)$$

where ξ is given by,

$$\xi = \frac{mv_f}{ne^2}, \quad (14)$$

In Eq. 14, m , v_f , n , and e are the effective mass, Fermi velocity, density, and charge of the carriers. As it is observed in Eq. 13, considering the $L \ll D_S$, i. e., the mean free path of the charge carriers is smaller than the grain diameter, this equation reduces to the Drude equation. In this model, L is given by [145,150],

$$L = \frac{L_{\text{ESM}} L_{\text{ISM}}}{L_{\text{ESM}} + L_{\text{ISM}}}, \quad (15)$$

where L_{ESM} is the elastic scattering mechanism, related to the acoustic phonon scattering [145,150] L_{ISM} is the inelastic scattering mechanism and is approximated by the following relation,

$$L_{\text{ISM}} = \chi T^{-p}. \quad (16)$$

In Eq. 16, χ is a proportional constant and p can vary from 0.8 up to 5, according to the temperature range and studied system. The β_G coefficient can be derived from this model and described by [145],

$$\beta_G = -\left(\frac{1}{L} + \frac{Ln(S)}{D_S}\right) \frac{dL}{dT}. \quad (17)$$

There are a number of reports using the Grain-boundary model to describe an experimental system with negative TCR. However, each study presents distinct approximations to reach a proper fit of the experimental data. The

results presented in [150] consider the p -value in the range of 2.5 up to 3 to describe the electrical resistivity of NbN thin films. On the other hand, for a similar system in which the NbN is Si-doped [150], the best fit of the experimental data was obtained using p in the range of 0.84 up to 1.15.

Focusing on the Grain-boundary model, a calculation of ρ_G as a function of temperature was performed, for distinct L_{ESM} and D_S values. Our goal here is to obtain the theoretical β_G value and to compare it with the experimental data. To this end, similar parameter values to that presented in [150] are considered, with $n \propto 10^{22} \text{ cm}^{-3}$ and $v_f \approx 1.2 \times 10^8 \text{ cm s}^{-1}$. Figure 15 (a) presents the temperature dependence of ρ_G for distinct values of grain-size (D_S). A similar plot is shown in Fig. 15 (b), which represents the temperature dependence of ρ_G for distinct values of the L_{ESM} . From these figures, it is verified a strong dependence of the curve's shapes by varying D_S and L_{ESM} in a few nm. In particular, the L/D ratio plays a critical role for the validity of the model, where $L/D > 1$ should be considered in the present case [150]. Using similar values employed previously in this work, Eq. 17 was used to infer β_G at room temperature. Considering $L_{\text{ESM}} = 10.5 \text{ nm}$ and $D_S = 2.3 \text{ nm}$, a value of $\beta_G = -6.4 \times 10^{-3} \text{ K}^{-1}$ is obtained. Further, by varying D_S to 3.0 nm , a considerable decrease of the $\beta_G = -4.6 \times 10^{-3} \text{ K}^{-1}$ is observed showing the important influence of the grains-size in the β_G coefficient.

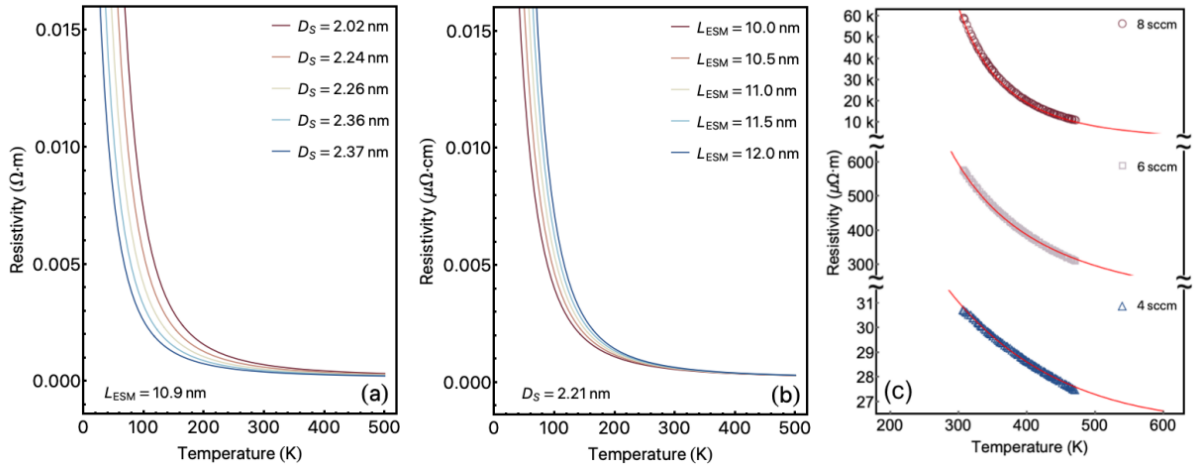


Figure 15: (a) ρ_G as a function of the temperature for distinct values of the grain-size (D_S). For this calculation, the following parameters are considered: $p = 1.04$, $S = 0.13$, $n = 40.4 \times 10^{23}$, and $\chi = 0.21 \times 10^4 \text{ nm}$. (b) Similar plot for $D_S = 2.21 \text{ nm}$ and distinct values of L_{ESM} . (c) Electrical resistivity measured for the CrN samples growth onto 8 (Blue), 6 (Red) and 4 (Black) sccm N_2 flux. The red line indicates the best fit, calculated from the grain-boundary model. The parameters used in this fit are shown in Tab.2.

The model has been further used to analyze the experimental results in order to obtain the β_G value of the samples, from the electrical resistivity. It is to notice that the experimental procedure led to varying columnar and grain-size parameters, modifying the mean free path of the charge carriers (L). In the following, the D_S values

have been considered as the crystallite size obtained from the XRD analysis, which are in the range of ≈ 22.6 nm, for N_2 flux of 4 sccm, up to ≈ 23 nm, for the system growth onto N_2 flux of 8 sccm. The best fit obtained from the model is presented in Fig. 15 (c). For the ρ_s calculation, the experimental results of the electrical resistivity measured in the temperature range from 300 up to 500 K are considered. Using Eq. 17, the theoretical β_G values at room temperature are obtained, as presented in Tab. 7, showing a good agreement between the experimental and theoretical data and thus confirming the suitability of the model to describe the observed behavior.

Table 7: Parameters employed in the scope of the grain-boundary model to describe the electrical resistivity depicted in the Fig.15. The β_G ($10^{-3} K^{-1}$) values are obtained/calculated at room temperature (293 K).

Parameter	4 sccm	6 sccm	8 sccm
ρ	1.04	1.04	1.04
χ (10^4 nm)	0.10	0.11	0.37
L_{ESM} (nm)	17.42	28.6.	60.8
S	0.030	0.0017	0.0012
D_S (nm)	22.5	23.5	23.7
β_G - Exp.($10^{-3} K^{-1}$)	-0.917	-5.31	-14.76
β_G - Theo. ($10^{-3} K^{-1}$)	-0.924	-5.18	-13.01

As a conclusion, and with the main goal to produce hard coatings based on chromium nitrides for temperature sensing applications, the relationship between the microstructure, deposited by DC-reactive magnetron sputtering under distinct amounts of nitrogen (N_2) tilting de deposition angle during the deposition, and the thermo-resistive response of CrN_x thin films through the TCR values has been obtained. Increasing grain size allows to increase the thermo-resistive response of CrN_x and, consequently, the TCR values. Thus, results show a way to explore the CrN_x system with negative TCR for the development of multifunctional high-performance hard coatings with temperature sensing characteristics.

4.2. Relative humidity sensor

4.2.1. Morphological and Structural Characterization

As mentioned before, porous nanostructures are potential candidates to be used as relative humidity sensors [151]. Fig. 16 shows the top and fractured cross-section view of the Cr-based thin films growth by PVD-GLAD with increasing N_2+O_2 flux, in order to evaluate the zigzag morphology and surface porosity.

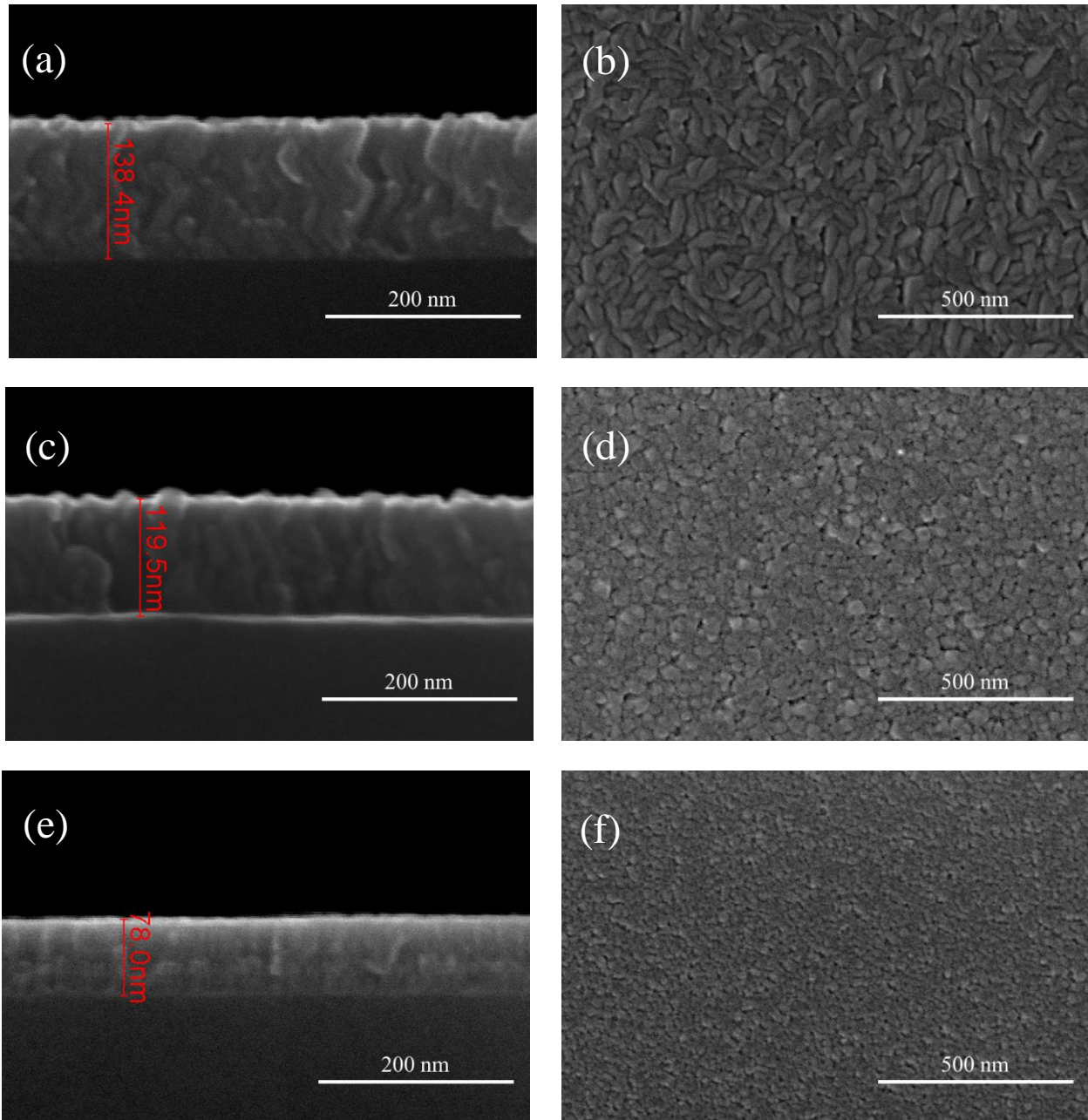
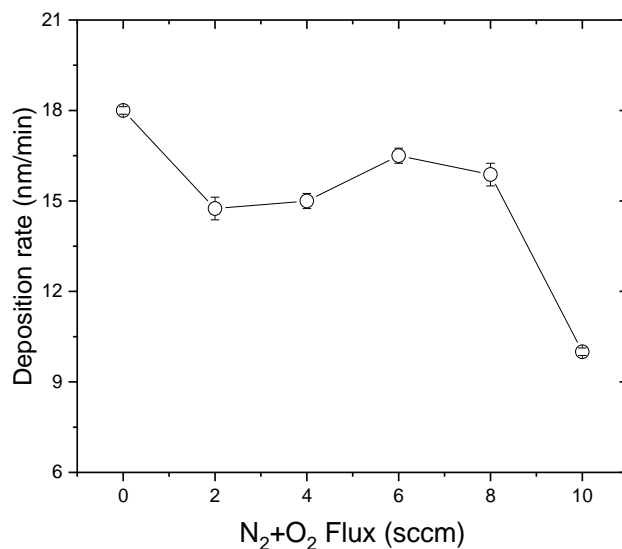


Figure 16: Representative SEM micrographs of the CrN_xO_y samples: a), c) and e) are the cross section views and b), d) and f) top views of the samples with N_2+O_2 flux of 0, 4 and 10 sccm, respectively.

Figure 16 shows that increasing N_2+O_2 flux during the PVD-GLAD growth process leads to morphological feature variations of the CrN_xO_y thin films, namely the columnar arrangement, including type, density, and surface characteristics. For pristine Cr thin films, well-defined zigzags structures were produced, Fig.16 a). By increasing the amount of reactive gas flux from 0 to 4 sccm, the zigzag columns become not well-defined and the surface gaps reveal a highly porous material, as detected on the films surface, Fig. 16 d). Increasing, even more, the reactive flux until 10 sccm leads to a vanishing of the zigzag structure and the porous structure is considerably reduced. With the successive increase of the reactive N_2+O_2 flux from pure Cr to 10 sccm of N_2+O_2 , the thickness of the produced columns decreases, from 138 nm to 78 nm, leading to a decrease of the grain boundaries, as observed in the surface images Fig. 16 b) and d).

Figure 17 a) shows the deposition rate of the samples processed by PVD-GLAD. For samples produced with a reactive flux from 2 to 8 sccm, the deposition rate is practically the same, around 15 nm/min, decreasing to approximately 10 nm/min for the samples produced with 10 sccm. This change in the deposition rate seems to be correlated with the zigzag growth since for higher deposition rates there is a better zigzag like structure and higher porosity, which disappear for low rates. Moreover, RBS results of the composition show a high level of O_2 ($\approx 16,5$ at %) in the samples produced without reactive gas, Figure 17 b). This fact can be attributed to the processing of the samples where the annealing protocol in-air from room temperature to a temperature of 200 °C can induce an oxidation layer on the surface of the samples [152]. Excluding the Cr sample, the addition of N_2+O_2 reactive gas leads to an increase in the amount of O_2 . Besides, the N_2 also shows initially the same trend than the O_2 up to a maximum of 4 sccm. After that, the presence of N_2 starts decreasing as the mixture flux increases. It is worth noting that although the mixture was composed by a ratio of $\sim 0,18$ O/N, increasing the amount of N_2+O_2 from 2 sccm to 10 sccm leads to an increase of the O/N ratio from 0.55 to 7.27. This behaviour is expected since oxygen shows a higher reactivity than nitrogen due to the chromium oxide higher binding enthalpy (-564 kJ/mol) when compared with chromium nitride (-125 kJ) [153,154], occupying the nitrogen position in the CrN_x lattice.

a)



b)

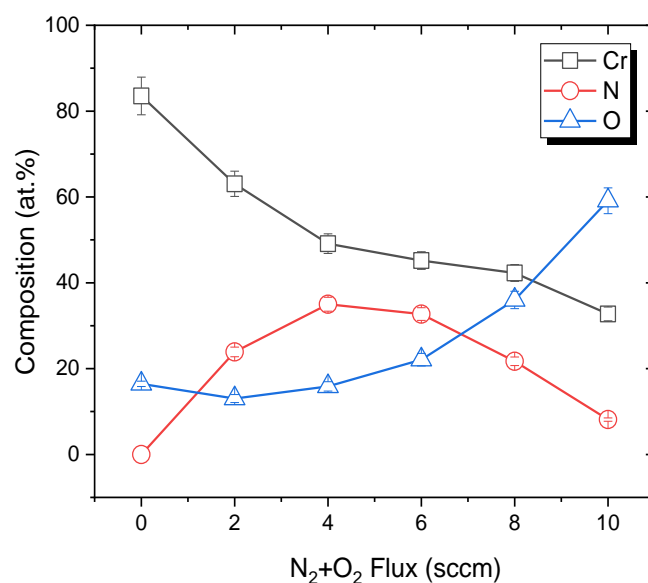


Figure 17: a) Deposition rate and b) elementary composition variation as a function of the N_2+O_2 flux.

In order to evaluate whether CrN_xO_y combines the properties of chromium nitride and chromium oxide like Cr_2O_3 , an XRD analysis was performed (Fig. 18). The results suggest that the $Cr(N, O)$ thin films are characterized by a polycrystalline structure. For the sample deposited without reactive flux, the diffractograms show a very intense Cr (210) peak located at $2\theta \approx 44.6^\circ$ and a smaller one at $2\theta \approx 64.8^\circ$ (310), related with a Cr-type with BCC cubic structure (ICSD card no. 00-001-1261). For the intermediate fluxes (2 and 4 sccm) the diffractograms show an amorphous structure with a broad band at $2\theta \approx 38.4^\circ$ and $2\theta \approx 44.8^\circ$, related to CrN (110) and CrN (002) diffraction peaks, respectively. For these fluxes, there seems to be a presence of both FCC and hcp CrN

phases that can be attributed to a Cr_2N ditrigonal scalenohedral crystalline structure (β - Cr_2N). For higher fluxes (6 to 8 sccm) an intense peak at 38.1° , FCC-CrN (111), and a smaller one at 64.0° , FCC-CrN (022) are observed. This transition from a BCC-Cr phase, a mixture of β - Cr_2N and FCC-CrN phase, are in agreement with the results related in [154,155].

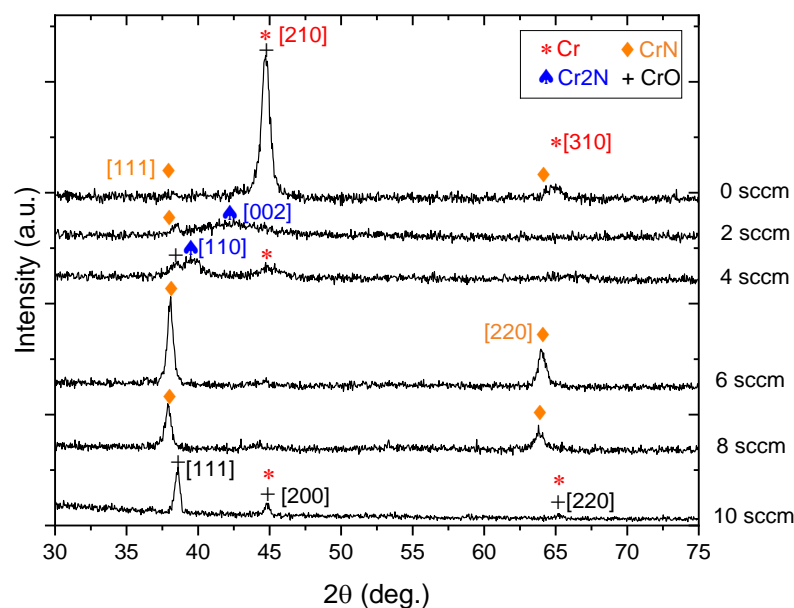


Figure 18: X-ray diffraction spectra of the CrN_xO_y samples.

By increasing the amount of N_2+O_2 to 10 sccm, the presence of the O_2 in the composition can be confirmed in the XRD results with the presence of a CrO crystalline structure, identified at $2\theta \approx 38.6^\circ$ and $2\theta \approx 44.8^\circ$ as well as the peak tail at $2\theta \approx 65^\circ$ (ICSD card no. 01-078-0722). The intense Cr peak located at $2\theta \approx 44.6^\circ$ and the weak CrO peak at $2\theta \approx 44.8^\circ$ probably consist of a mixture of both Cr and CrO phases [156]. The oxygen may be integrated into the CrN cubic structure partially substituting the N atoms at low percentages since CrO is only known to crystallize at a temperature above 400°C or at oxygen atomic percentages above 40 at.% [36,157,158] which are in agreement with our results. The fact of the Cr has been prepared in a metal phase by the reactive sputtering method, the addition of N_2+O_2 in a first step induces a nitrification process in the produced coatings and, in a second step, the amount of O_2 becomes most reactive than nitrogen producing chromium oxide.

4.2.2. Electrical properties

The electrical resistivity of the films (Fig. 19), a key factor for the suitability of the developed materials for sensing applications, was determined at room temperature. The obtained electrical resistivity values allow to categorize the CrN_xO_y coatings into three different regimes, as represented in Fig. 19. The thin films prepared without reactive flux (absence of O_2) revealed low electrical resistivity values ($1.27 \times 10^{-6} \pm 5.02 \times 10^{-8}$) (Zone I), typical of a common metallic-like behavior [159], even when the RBS results demonstrate a presence of O_2 around 16.5 at.%, as a result of the annealing protocol [152]. The Zone II correspond to the coatings prepared with intermediate reactive flux and is characterized by intermediate electrical resistivity values, increasing from $2.43 \times 10^{-6} \pm 4.54 \times 10^{-8} \Omega\cdot\text{m}$ to $3.80 \times 10^{-2} \pm 6.20 \times 10^{-6} \Omega\cdot\text{m}$, which can be indexed to a semiconductor type of response. Finally, the samples produced with the highest oxygen contents (Zone III) show higher resistivity values (in the order of $4.50 \times 10^9 \pm 4.20 \times 10^7 \Omega\cdot\text{m}$), typical of an insulator-type behavior.

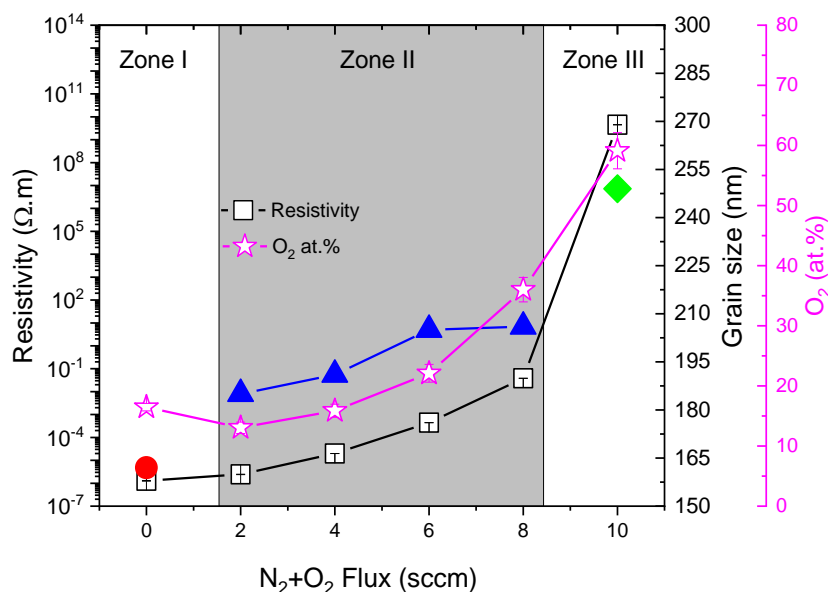


Figure 19: Room temperature resistivity, grain size and amount of O_2 as a function of the N_2+O_2 reactive flux.

The electrical resistivity is the result of various scattering processes that can be interpreted in terms of the Mayadas-Shatzkes theory [149]. Thin films often present an island or grain-like structures, showing thus a discontinuous morphology. When these grains or islands show dimensions on the order of the conduction electron mean free path, the scattering at the grain boundaries leads to a very high resistivity. In fact, and using the Debye-Scherrer method [141] to determine the crystalline size of the coating from XRD results, it is shown that by shifting from the lacking to the overload oxygen content zone (Fig. 19): a) the grain size increases from ≈ 191 nm up to ≈ 249 nm, b) the amount of oxygen in the coatings increases from ≈ 16.5 at.% to ≈ 59.1 at.%, and c)

the grain boundaries become denser, Fig. 16 f). It can be assumed that the contribution to the electrical resistivity by the grain boundaries and oxygen concentration is larger than the contribution of the grains size.

4.2.3. Relative Humidity Sensing Characteristics

Taking into account the main goal of this work, the CrN_xO_y coatings prepared with different amounts of N_2+O_2 were evaluated through the resistance variation as a function of relative humidity (RH) variation from $\approx 40\%$ to near 90% at a constant temperature of 25°C . The repeatability is addressed in Fig. 20, which shows the measured electrical resistance plotted versus relative humidity cyclic variation. The black dots represent the raw data. These data represent four cycles of ultrasonic humidifier on-off switch beaker with distilled water. The purple line represents the raw data from a commercial sensor acquired from a commercial datalogger (Amprobe TR200-A).

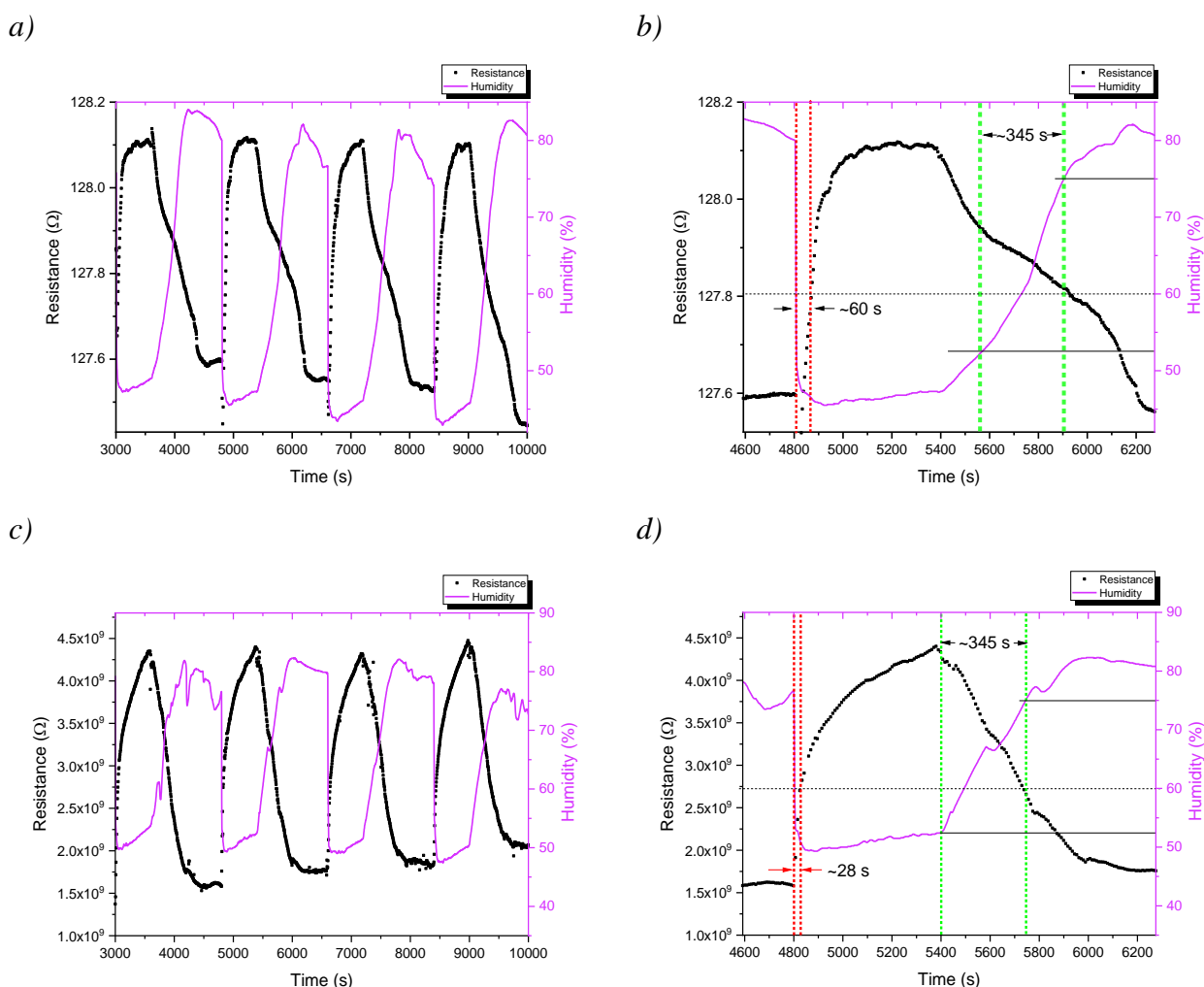


Figure 20: Sensor response characterization by the electrical resistance variation with the relative humidity for the samples deposited with a flux of N_2+O_2 of: a) 4 sccm, c) 10 sccm and the corresponding magnifications b) and d) for a single cycle.

Fig. 20b and d show the time response and recovery of the CrN_xO_y thin films and the signal response of the commercial humidity sensor. The response times are defined here as the time it takes for the signal to reach from $\approx 52\%$ of the initial humidity value to 75% of the final humidity value. The recovery times are defined as the time it takes for the signal to reach from $\approx 80\%$ of the initial humidity value to 60% of the final humidity value. The regions are marked with dashed green and red lines in Fig. 20, respectively. The measured response times are 345 s for both systems produced with a flux of N_2+O_2 of 4 sccm, Fig. 20 b), and 10 sccm, Fig. 20 d). The recovery time decreases from 60 s to 28 s with increasing amount of O_2 in the CrN_xO_y system. The combination of these measurements shows that the response and recovery times of the devices are on the order of seconds and are possibly much faster than observed due to the limited response time of the experimental setup. However, if we compare the electrical evolution of the samples with increasing N_2+O_2 fluxes, Fig. 20 a) and c), the CrN_xO_y thin films react to the humidity, decreasing the electrical resistance with increasing relative humidity and the time response decreases with increasing O_2 in the composition, which suggests higher sensibility to the humidity.

Thus, Eq. 12 allows to determine the sensor response of the CrN_xO_y films in the presence of humidity. The results are presented in Fig. 20.

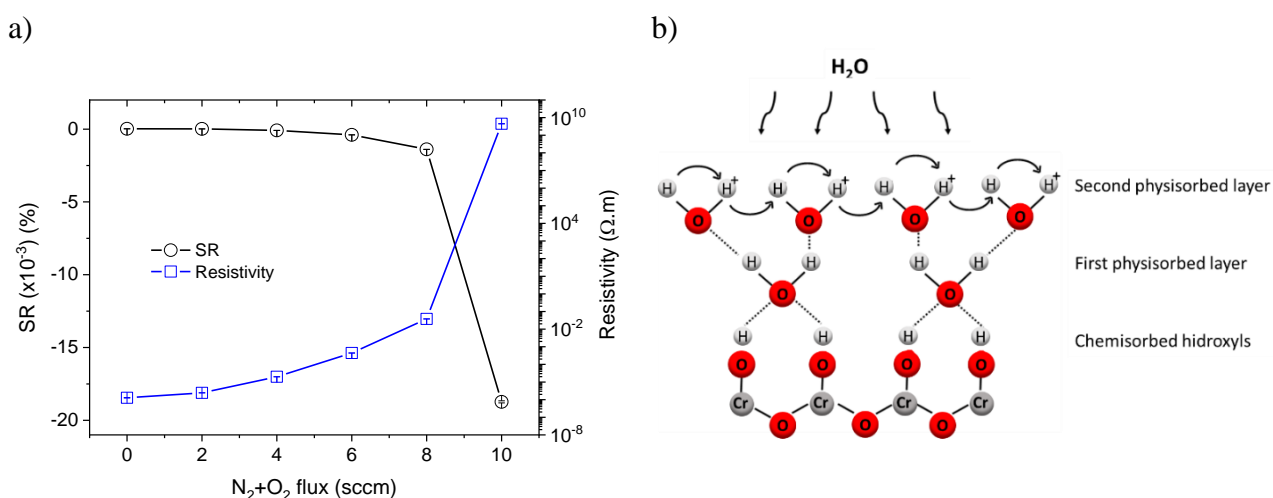


Figure 21: a) Electrical resistivity and ΔRH as a function of the N_2+O_2 flow rate applied during the reactive sputtering of the CrN_xO_y samples, b) adsorbed layers on a high humidity environment.

Figure 21 shows that the lowest SR values are obtained for the lower N_2+O_2 flow rates (0 and 2 sccm). For chromium samples (0 sccm), the sensibility shows a value of $\text{SR} = 2.36 \times 10^{-5} \pm 3.00 \times 10^{-7} (\text{RH} \%)^{-1}$, in the same order than the sample prepared with 2 sccm of N_2+O_2 flux ($\text{SR} = 1.68 \times 10^{-5} \pm 1.30 \times 10^{-6} (\text{RH} \%)^{-1}$). The low value can be attributed to the low electrical resistance and due to the fact that Cr was prepared in a metal phase. For N_2+O_2

flow rates of 4 to 10 sccm, the electrical resistivity increases and the highest negative SR values of $8.56 \times 10^{-5} \pm 6.00 \times 10^{-7}$ to $1.87 \times 10^{-2} \pm 7.00 \times 10^{-5}$ (RH %)⁻¹ are obtained, confirming the highest time response of the system with higher O₂ concentration.

The relative humidity sensitivity is closely related to the concentration of water adsorption sites and since CrN is hydrophobic and oxides are hydrophilic, the relative humidity sensitivity increases in the presence of O₂ [4] as verified in our study. The behaviour of the humidity in the samples will influence the number of adsorbed layers of water [4,48], as represented in Fig. 21 b). For low humidity environments, only a chemisorbed layer of hydroxyl ions will be present at the oxide surface, resulting from the water ionization reaction of the water vapor, in which the water loses one H⁺ atoms forming surface hydroxide ions (OH⁻). The presence of water molecules and OH⁻ into the surface, covering the surface, lead to proton H⁺ charge carriers, occurring the proton migration by hopping between adjacent OH sites, which promotes a decrease in the electrical resistivity of the sample as a result of the quantum tunnelling of electrons between neighbouring water molecules [4]. After the hydroxyl group formation, and with increasing humidity, the next water molecule layer is physisorbed (Fig. 21) by hydrogen double bonds on hydroxyl groups in which a proton is transferred from a hydroxyl group forming an H₃O⁺ ion. For even higher humidity levels, water will be able to condense in the capillary sites of the surface, increasing the electrolytic conduction by proton hopping, being the protons able to tunnel between adjacent water particles [4].

In this sense, the sensibility of the films should be attributed not only to the presence of oxygen in the CrN_xO_y coatings but also to the porosity present in the surface of the coatings, Fig. 16, which will facilitate the adsorption of water vapor on its lower layers giving great scope for enhancement in the sensitivity of the relative humidity sensors.

As a conclusion, coatings based on chromium oxynitrides have been developed for humidity sensing applications by tailoring thin film microstructure and composition. Increasing the amount of O₂ in the composition allows to increase the sensitivity to the humidity response of CrN_xO_y and, consequently, the SR values. Thus, the results show a way to explore the CrN_xO_y system with negative SR for the development of multifunctional high-performance coatings with humidity sensing characteristics.

5. Conclusions

Thin film chromium nitride samples and chromium oxynitride samples were successfully synthesized by GLAD assisted DC reactive magnetron sputtering.

The samples of chromium nitride allowed a set of conclusions:

- Nitrogen increased on the samples as the nitrogen flux increased on the deposition process.
- As the flux of nitrogen increases the structure of the samples changes from a Cr-BCC structure to a CrN-FCC structure with the coexistence with a Cr₂N hexagonal structure at lower nitrogen fluxes. The increase in nitrogen flux also promotes the increase of the grain size of the samples.
- The GLAD process promotes a zigzag microstructure on the sample. Porosity is also observed.
- It has been found a negative TCR coefficient for the thin films produced with N₂ flux of 4, 6 and 8 sccm, which correlates with the variation of the morphological features, namely in the columnar arrangement (type, density, hardness and surface aspect) and with the transition from Cr to CrN_x cubic phase. Besides, the thermoresistivity showed very stable behavior as a function of both temperature and time. Further, the grain-boundary model allows calculating the β_G coefficients theoretically, which are in agreement with the experimental ones, and therefore allow to disclose the physical mechanism behind the obtained response.
- Our results pave the way to explore the CrN_x system with negative TCR for the development of multifunctional high-performance hard coatings with temperature sensing characteristics.

On the other hand, the conclusions achieved by the characterization of the chromium oxynitride samples were:

- The increase of the N₂+O₂ flux during the deposition of the Cr process increased the atomic percentage of N₂+O₂ on the samples. More, this increase also provoked an increase of O/N ratio due to the higher reactivity of the oxygen when compared with the nitrogen reactivity.
- The addition of N₂+O₂ produces, for lower fluxes, chromium nitride coatings. On the other hand, for higher fluxes, the formation of chromium oxide is induced due to the high oxygen reactivity.
- SEM images showed granular samples with high porosity with zigzag growth, this structure was more present on samples deposited with 4, 6 and 8 sccm of N₂+O₂ mixture flow. The deposition rate was lower in the 10 sccm deposited sample and was approximately the same to all other samples.

- The amount of O_2 present in the composition of the coatings leads to high electrical resistivity and increase the relative sensitivity.
- The films deposited with high N_2+O_2 flux show a higher sensor response to humidity. The sensibility of the films should be attributed not only to the presence of oxygen in the CrN_xO_y coatings but also to the porosity presented in the surface of the coatings, which promote the adsorption of water vapor on its lower layers, allowing the improvement of the sensitivity of the sensors.

6. Future work

The obtained results of this work allow us to open new lines of study and mechanisms for the future. The inclusion of nitrogen and oxygen into chromium matrices has shown to be advantageous in creating a temperature and humidity transducer. Further investigation needs optimization and calibration in this array of sensors. The implementation of a functional prototype with integrated sensor calibrated, as well with various environmental conditions is also needed.

New thin films with different transition metals should also be considered and produced with inclined columns and spirals by Glancing Angle Deposition technique. The GLAD architectures (zig-zags) have brought excellent thermoresistive and humidity responses, with promising results for sensor devices applications. The possibility to sculpture the Cr-based thin films will expand the possibilities to control the material, at the nanometer scale, and hence to enhance the elasticity of the films deposited on flexible-like polymers.

The obtained results also raise the possibility of upscaling these materials for use into a production scale.

7. References

- [1] Z. Huang, J. Lin, D. Lv, High-precision Monitoring and Controlling System of Temperature and Humidity Based on CAN Bus, *Appl. Mech. Mater.* 148–149 (2012) 1280–1284. <https://doi.org/10.4028/www.scientific.net/AMM.148-149.1280>.
- [2] M. Hermann, T. Pentek, B. Otto, Design principles for industrie 4.0 scenarios, in: T.X. Bui, R.H.S. Jr (Eds.), *Proc. Annu. Hawaii Int. Conf. Syst. Sci.*, IEEE Computer Society Conference Publishing Services, Hawaii, 2016: pp. 3928–3937. <https://doi.org/10.1109/HICSS.2016.488>.
- [3] R.H. Todd, D.K. Allen, L. Alting, *Manufacturing Processes Reference Guide*, 1st ed., Industrial Press, New York, 1994. https://books.google.pt/books?id=6x1smAf_PAAC.
- [4] G. Korotcenkov, *Handbook of Humidity Measurement, Volume 2: Electronic and Electrical Humidity Sensors*, 1st ed., CRC Press, New York, 2019. <https://doi.org/10.1201/b22370>.
- [5] A. Ferreira, J.P. Silva, R. Rodrigues, N. Martin, S. Lanceros-Méndez, F. Vaz, High performance piezoresistive response of nanostructured ZnO/Ag thin films for pressure sensing applications, *Thin Solid Films*. 691 (2019) 137587. <https://doi.org/10.1016/j.tsf.2019.137587>.
- [6] E. Oliveira, J.P. Silva, J. Laranjeira, F. Macedo, S. Lanceros-Mendez, F. Vaz, A. Ferreira, Fabrication, characterization and implementation of thermo resistive TiCu(N, O) thin films in a polymer injection mold, *Materials (Basel)*. 13 (2020) 1423. <https://doi.org/https://doi.org/10.3390/ma13061423>.
- [7] J. Musil, P. Baroch, J. Vlček, K.H. Nam, J.G. Han, Reactive magnetron sputtering of thin films: Present status and trends, *Thin Solid Films*. 475 (2005) 208–218. <https://doi.org/10.1016/j.tsf.2004.07.041>.
- [8] M.T. Taschuk, M.M. Hawkeye, M.J. Brett, Glancing Angle Deposition, in: P.M. Martin (Ed.), *Handb. Depos. Technol. Film. Coatings*, 3rd ed., Elsevier Inc, Oxford, 2010: pp. 621–678. <https://doi.org/10.1016/B978-0-8155-2031-3.00013-2>.
- [9] T.G. Knorr, R.W. Hoffman, Dependence of geometric magnetic anisotropy in thin iron films, *Phys. Rev.* 113 (1959) 1039–1046. <https://doi.org/10.1103/PhysRev.113.1039>.
- [10] S. Qiao, X. Peng, L. Wang, S. Duan, J. Chu, P. Jia, Highly sensitive humidity sensor based on oblique carbon nanoplumes, *Sensors (Switzerland)*. 18 (2018) 3407. <https://doi.org/10.3390/s18103407>.
- [11] H.O. Chu, S. Song, C. Li, D. Gibson, Surface enhanced Raman scattering substrates made by oblique angle deposition: Methods and applications, *Coatings*. 7 (2017) 26.

<https://doi.org/10.3390/coatings7020026>.

- [12] A. Ferreira, P. Pedrosa, N. Martin, M.A.P. Yazdi, A. Billard, S. Lanceros-Méndez, F. Vaz, Nanostructured $\text{Ti}_{1-x}\text{Cu}_x$ thin films with tailored electrical and morphological anisotropy, *Thin Solid Films*. 672 (2019) 47–54. <https://doi.org/10.1016/j.tsf.2019.01.008>.
- [13] P. Pedrosa, A. Ferreira, N. Martin, M. Arab Pour Yazdi, A. Billard, S. Lanceros-Méndez, F. Vaz, Nano-sculptured Janus-like TiAg thin films obliquely deposited by GLAD co-sputtering for temperature sensing, *Nanotechnology*. 29 (2018). <https://doi.org/10.1088/1361-6528/aacba8>.
- [14] Q. Wang, F. Zhou, J. Yan, Evaluating mechanical properties and crack resistance of CrN, CrTiN, CrAlN and CrTiAlN coatings by nanoindentation and scratch tests, *Surf. Coatings Technol.* 285 (2016) 203–213. <https://doi.org/10.1016/j.surfcoat.2015.11.040>.
- [15] Y.C. Chim, X.Z. Ding, X.T. Zeng, S. Zhang, Oxidation resistance of TiN, CrN, TiAlN and CrAlN coatings deposited by lateral rotating cathode arc, *Thin Solid Films*. 517 (2009) 4845–4849. <https://doi.org/10.1016/j.tsf.2009.03.038>.
- [16] E.Y. Choi, M.C. Kang, D.H. Kwon, D.W. Shin, K.H. Kim, Comparative studies on microstructure and mechanical properties of CrN, Cr-C-N and Cr-Mo-N coatings, *J. Mater. Process. Technol.* 187–188 (2007) 566–570. <https://doi.org/10.1016/j.jmatprotec.2006.11.090>.
- [17] A. Gilewicz, P. Chmielewska, D. Murzynski, E. Dobruchowska, B. Warcholinski, Corrosion resistance of CrN and CrCN/CrN coatings deposited using cathodic arc evaporation in Ringer's and Hank's solutions, *Surf. Coatings Technol.* 299 (2016) 7–14. <https://doi.org/https://doi.org/10.1016/j.surfcoat.2016.04.069>.
- [18] S.K. Singh, S. Chattopadhyaya, A. Pramanik, S. Kumar, Wear behavior of chromium nitride coating in dry condition at lower sliding velocity and load, *Int. J. Adv. Manuf. Technol.* 96 (2018) 1665–1675. <https://doi.org/10.1007/s00170-017-0796-x>.
- [19] M. Arif, A. Sanger, A. Singh, Sputter deposited chromium nitride thin electrodes for supercapacitor applications, *Mater. Lett.* 220 (2018) 213–217. <https://doi.org/10.1016/j.matlet.2018.02.094>.
- [20] D. Ross-Pinnock, P.G. Maropoulos, Identification of key temperature measurement technologies for the enhancement of product and equipment integrity in the light controlled factory, *Procedia CIRP*. 25 (2014) 114–121. <https://doi.org/10.1016/j.procir.2014.10.019>.
- [21] A. Ferreira, N. Martin, S. Lanceros-Méndez, F. Vaz, Tuning electrical resistivity anisotropy of ZnO thin films

- for resistive sensor applications, *Thin Solid Films*. 654 (2018) 93–99.
<https://doi.org/10.1016/j.tsf.2018.03.090>.
- [22] A. Ferreira, J. Borges, C. Lopes, M.S. Rodrigues, S. Lanceros-Mendez, F. Vaz, Relationship between nano-architected $\text{Ti}_{1-x}\text{Cu}_x$ thin film and electrical resistivity for resistance temperature detectors, *J. Mater. Sci.* 52 (2017) 4878–4885. <https://doi.org/10.1007/s10853-016-0722-x>.
- [23] M.J.M. Jimenez, V. Antunes, S. Cucatti, A. Riul, L.F. Zagonel, C.A. Figueroa, D. Wisnivesky, F. Alvarez, Physical and micro-nano-structure properties of chromium nitride coating deposited by RF sputtering using dynamic glancing angle deposition, *Surf. Coatings Technol.* 372 (2019) 268–277.
<https://doi.org/10.1016/j.surfcoat.2019.05.023>.
- [24] H.M. Hashemian, W.C. Bean, State-of-the-art predictive maintenance techniques, *IEEE Trans. Instrum. Meas.* 60 (2011) 3480–3492. <https://doi.org/10.1109/TIM.2009.2036347>.
- [25] C. Gautier, J. Machet, Study of the Growth Mechanisms and Properties of (Cr,O,N) Films Deposited by Vacuum Arc Evaporation, *Mater. Sci. Forum.* 287–288 (1998) 393–396.
<https://doi.org/10.4028/www.scientific.net/MSF.287-288.393>.
- [26] A. Besnard, N. Martin, L. Carpentier, B. Gallas, A theoretical model for the electrical properties of chromium thin films sputter deposited at oblique incidence, *J. Phys. D. Appl. Phys.* 44 (2011) 215301.
<https://doi.org/10.1088/0022-3727/44/21/215301>.
- [27] A. Ferreira, C. Lopes, N. Martin, S. Lanceros-Méndez, F. Vaz, Nanostructured functional Ti-Ag electrodes for large deformation sensor applications, *Sensors Actuators, A Phys.* 220 (2014) 204–212.
<https://doi.org/10.1016/j.sna.2014.09.031>.
- [28] P. Pedrosa, C. Lopes, N. Martin, C. Fonseca, F. Vaz, Electrical characterization of Ag:TiN thin films produced by glancing angle deposition, *Mater. Lett.* 115 (2014) 136–139.
<https://doi.org/10.1016/j.matlet.2013.10.044>.
- [29] A. Ferreira, J. Borges, C. Lopes, N. Martin, S. Lanceros-Mendez, F. Vaz, Piezoresistive response of nano-architected Ti_xCu_y thin films for sensor applications, *Sensors Actuators, A Phys.* 247 (2016) 105–114.
<https://doi.org/10.1016/j.sna.2016.05.033>.
- [30] J.M.D. Coey, A.E. Berkowitz, L.I. Balcells, F.F. Putris, A. Barry, Magnetoresistance of chromium dioxide powder compacts, *Phys. Rev. Lett.* 80 (1998) 3815–3818.
<https://doi.org/10.1103/PhysRevLett.80.3815>.

- [31] I. Batko, M. Batkova, F. Lofaj, Electrical resistivity of CrN thin films, *Acta Phys. Pol. A.* 126 (2014) 415–416. <https://doi.org/10.12693/APhysPolA.126.415>.
- [32] M.D. Julkarnain, J. Hossain, K.S. Sharif, K.A. Khan, Temperature effect on the electrical properties of chromium oxide (Cr_2O_3) thin films, *J. Optoelectron. Adv. Mater.* 13 (2011) 485–490.
- [33] P. Hones, M. Diserens, F. Lévy, Characterization of sputter-deposited chromium oxide thin films, *Surf. Coatings Technol.* 120–121 (1999) 277–283. [https://doi.org/10.1016/S0257-8972\(99\)00384-9](https://doi.org/10.1016/S0257-8972(99)00384-9).
- [34] M.F. Al-Kuhaili, S.M.A. Durrani, Optical properties of chromium oxide thin films deposited by electron-beam evaporation, *Opt. Mater. (Amst.)* 29 (2007) 709–713. <https://doi.org/10.1016/j.optmat.2005.11.020>.
- [35] K. Suzuki, H. Suematsu, G. James, T. Suzuki, Microstructure of Cr (N,O) thin films studied by high resolution transmission electron microscopy, *Thin Solid Films.* 625 (2017) 111–114. <https://doi.org/10.1016/j.tsf.2017.01.062>.
- [36] J. Shirahata, T. Ohori, H. Asami, T. Suzuki, T. Nakayama, H. Suematsu, S.W. Lee, Z. Fu, K. Niihara, Influence of oxygen content on hardness of Cr(N,O) thin films deposited by an RF sputtering method, *IOP Conf. Ser. Mater. Sci. Eng.* 20 (2011) 012005. <https://doi.org/10.1088/1757-899X/20/1/012005>.
- [37] T. Wierzchoń, I. Ulbin-Pokorska, K. Sikorski, Corrosion resistance of chromium nitride and oxynitride layers produced under glow discharge conditions, *Surf. Coatings Technol.* 130 (2000) 274–279. [https://doi.org/10.1016/S0257-8972\(00\)00696-4](https://doi.org/10.1016/S0257-8972(00)00696-4).
- [38] H.C. Bolton, Evolution of the Thermometer, 1592–1743, *Nature.* 64 (1901) 25–26. <https://doi.org/10.1038/064025a0>.
- [39] R.P. Benedict, *Fundamentals of Temperature, Pressure, and Flow Measurements*, 3rd ed., John Wiley & Sons, Inc, New York, 1984. <https://doi.org/10.1002/9780470172698>.
- [40] G.K. McMillan, *Advanced Temperature Measurement and Control*, 2nd ed., ISA, Research Triangle Park, NC 27709, 2010.
- [41] M. Nau, *Electrical temperature measurement: with thermocouples and resistance thermometers*, 10th ed., Juchheim, Fulda, 2002.
- [42] C.M. Jha, ed., *Thermal Sensors*, Springer, New York, 2015. <https://doi.org/10.1007/978-1-4939-2581-0>.
- [43] THERMISTOR BASICS – Wavelength Electronics, (n.d.). <https://www.teamwavelength.com/thermistor->

basics/ (accessed January 14, 2021).

- [44] L. Michalski, K. Eckersdorf, J. Kucharski, J. McGhee, L. Michalski, Temperature measurement, 2nd ed., JOHN WILEY & SONS, LTD, Chichester, 2001. <https://doi.org/10.1002/0470846135>.
- [45] J. Kucharski, Thermocouple Temperature Sensors, in: P.H. Sydenham, R. Thorn (Eds.), Handb. Meas. Syst. Des., 1st ed., Wiley, New Jersey, 2005: pp. 1315–1321. <https://doi.org/https://doi.org/10.1002/0471497398.mm293>.
- [46] R.Y. Goshlya, S.S. Busarov, A.Y. Gromov, A. V. Nedovenchany, I.S. Busarov, The Application of Compact Thermistors for the Temperature Conditions Analysis of Small-sized Long-stroke Low-speed Stages of Piston Compressors, *Procedia Eng.* 152 (2016) 281–287. <https://doi.org/10.1016/j.proeng.2016.07.704>.
- [47] E. Kohn, SiC thin-film thermistor, *Thin Solid Films.* 125 (1985) 355–359. [https://doi.org/10.1016/0040-6090\(85\)90244-5](https://doi.org/10.1016/0040-6090(85)90244-5).
- [48] H. Farahani, R. Wagiran, M.N. Hamidon, Humidity sensors principle, mechanism, and fabrication technologies: A comprehensive review, *Sensors.* 14 (2014) 7881–7939. <https://doi.org/10.3390/s140507881>.
- [49] P. Su, L. Huang, Humidity sensors based on TiO₂ nanoparticles / polypyrrole composite thin films, *Sensors Actuators, B Chem.* 123 (2007) 501–507. <https://doi.org/10.1016/j.snb.2006.09.052>.
- [50] H.L. Penman, Humidity, 1st ed., Institute of Physics, Michigan, 1955. <https://doi.org/https://doi.org/10.1002/qj.49708235220>.
- [51] G. Korotcenkov, Handbook of Humidity Measurement, Volume 1: Spectroscopic Methods of Humidity Measurement, 1st ed., CRC Press, New York, 2019.
- [52] G. Korotcenkov, Handbook of Humidity Measurement, volume 3: Methods, Materials and Technologies, 1st ed., CRC Press, New York, 2019.
- [53] E. Traversa, Ceramic sensors for humidity detection: the state-of-the-art and future developments, *Sensors Actuators B. Chem.* 23 (1995) 135–156. [https://doi.org/10.1016/0925-4005\(94\)01268-M](https://doi.org/10.1016/0925-4005(94)01268-M).
- [54] T. Nitta, Development and Application of Ceramic Humidity Sensors, in: Tetsuro SEIYAMA (Ed.), Chem. Sens. Technol. Vol. 1, 1st ed., ELSEVIER SCIENCE PUBLISHERS B. V, Amsterdam, 1988: pp. 57–78. <https://doi.org/10.1016/B978-0-444-98901-7.50009-9>.
- [55] Y. Sakai, Ion Conducting Polymer Sensors, in: Y. Osada, D.E. De Rossi (Eds.), Polym. Sensors Actuators,

1st ed., Springer, Berlin, Germany, 2000: pp. 1–14.

- [56] Y. Sakai, M. Matsuguchi, N. Yonesato, Humidity sensor based on alkali salts of poly (2-acrylamido-2-methylpropane sulfonic acid), *Electrochim. Acta.* 46 (2001) 1509–1514. [https://doi.org/https://doi.org/10.1016/S0013-4686\(00\)00746-5](https://doi.org/https://doi.org/10.1016/S0013-4686(00)00746-5).
- [57] M. Hijikigawa, S. Miyoshi, T. Sugihara, A. Jinda, A thin-film resistance humidity sensor, *Sensors and Actuators.* 4 (1983) 307–315. [https://doi.org/https://doi.org/10.1016/0250-6874\(83\)85038-0](https://doi.org/https://doi.org/10.1016/0250-6874(83)85038-0).
- [58] I. Fratoddi, A. Bearzotti, I. Venditti, C. Cametti, M. V Russo, Sensors and Actuators B : Chemical Role of nanostructured polymers on the improvement of electrical response-based relative humidity sensors, *Sensors Actuators B. Chem.* 225 (2016) 96–108. <https://doi.org/10.1016/j.snb.2015.11.001>.
- [59] C. Zhu, F. Xu, L. Zhang, M. Li, J. Chen, S. Xu, Ultrafast Preparation of Black Phosphorus Quantum Dots for Efficient Humidity Sensing, *Chem. A Eur. J.* 22 (2016) 7357–7362. <https://doi.org/10.1002/chem.201600719>.
- [60] P. Yasaei, A. Behranginia, T. Foroozan, M. Asadi, K. Kim, Stable and Selective Humidity Sensing Using Stacked Black Phosphorus Flakes, *ACS Nano.* 9,10 (2015) 9898–9905. <https://doi.org/https://doi.org/10.1021/acsnano.5b03325>.
- [61] D. Phan, I. Park, A. Park, C. Park, K. Jeon, Black P / graphene hybrid : A fast response humidity sensor with good reversibility and stability, *Sci. Rep.* 7 (2017) 10561. <https://doi.org/10.1038/s41598-017-10848-3>.
- [62] W. Chen, J. Huang, C. Zhu, Q. Huang, A Black Phosphorus humidity sensor with High Sensitivity and Fast Response, in: 2016 IEEE SENSORS, Orlando, FL, USA, 2016: pp. 1–3. <https://doi.org/10.1109/ICSENS.2016.7808462>.
- [63] A.D. Smith, K. Elgammal, F. Niklaus, A. Delin, A.C. Fischer, S. Vaziri, F. Forsberg, M. Rålander, H. Hugosson, L. Bergqvist, S. Schröder, S. Kataria, Resistive graphene humidity sensors with rapid and direct electrical readout †, *R. Soc. Chem.* 7 (2015) 19099–19109. <https://doi.org/10.1039/c5nr06038a>.
- [64] J. Lee, D. Cho, Y. Jeong, A resistive-type sensor based on flexible multi-walled carbon nanotubes and polyacrylic acid composite films, *Solid. State. Electron.* 87 (2013) 80–84. <https://doi.org/10.1016/j.sse.2013.05.001>.
- [65] A.S. Berdinsky, Y. V Shevtsov, A. V Okotrub, S. V Trubin, L.T. Chadderton, D. Fink, J.H. Lee, Sensor Properties of Fullerene Films and Fullerene Compounds with Iodine, *Chem. Sustain. Dev.* 8 (2000) 141–

- [66] A.S. Afify, S. Ahmad, R.A. Khushnood, P. Jagdale, J.M. Tulliani, Elaboration and characterization of novel humidity sensor based on micro-carbonized bamboo particles, *Sensors Actuators, B Chem.* 239 (2017) 1251–1256. <https://doi.org/10.1016/j.snb.2016.09.130>.
- [67] A. Kromka, M. Davydova, B. Rezek, M. Vanecek, M. Stuchlik, P. Exnar, M. Kalbac, Gas sensing properties of nanocrystalline diamond films, *Diam. Relat. Mater.* 19 (2010) 196–200. <https://doi.org/10.1016/j.diamond.2009.10.006>.
- [68] L. Du, Y. Zhang, Y. Lei, H. Zhao, Synthesis of high-quality CdS nanowires and their application as humidity sensors, *Mater. Lett.* 129 (2014) 46–49. <https://doi.org/10.1016/j.matlet.2014.05.002>.
- [69] R. Demir, S. Okur, M. Şeker, Electrical characterization of CdS nanoparticles for humidity sensing applications, *Ind. Eng. Chem. Res.* 51 (2012) 3309–3313. <https://doi.org/10.1021/ie201509a>.
- [70] S. Okur, N. Üzar, N. Tekgüzel, A. Erol, M. Çetin Arkan, Synthesis and humidity sensing analysis of ZnS nanowires, *Phys. E Low-Dimensional Syst. Nanostructures.* 44 (2012) 1103–1107. <https://doi.org/10.1016/j.physe.2010.08.015>.
- [71] N. Üzar, S. Okur, M.Ç. Arikan, Investigation of humidity sensing properties of ZnS nanowires synthesized by vapor liquid solid (VLS) technique, *Sensors Actuators, A Phys.* 167 (2011) 188–193. <https://doi.org/10.1016/j.sna.2010.10.005>.
- [72] Y.P. Leung, W.C.H. Choy, T.I. Yuk, Linearly resistive humidity sensor based on quasi one-dimensional ZnSe nanostructures, *Chem. Phys. Lett.* 457 (2008) 198–201. <https://doi.org/10.1016/j.cplett.2008.04.005>.
- [73] G. Dražič, M. Trontelj, Preparation and properties of ceramic sensor elements based on MgCr_2O_4 , *Sensors and Actuators.* 18 (1989) 407–414. [https://doi.org/10.1016/0250-6874\(89\)87046-5](https://doi.org/10.1016/0250-6874(89)87046-5).
- [74] Y. Yokomizo, S. Uno, M. Harata, H. Hiraki, K. Yuki, Microstructure and humidity-sensitive properties of $\text{ZnCr}_2\text{O}_4\text{-LiZnVO}_4$ ceramic sensors, *Sensors and Actuators.* 4 (1983) 599–606. [https://doi.org/10.1016/0250-6874\(83\)85073-2](https://doi.org/10.1016/0250-6874(83)85073-2).
- [75] K.C. Sajjan, A.S. Roy, A. Parveen, S. Khasim, Analysis of DC and AC properties of a humidity sensor based on polyaniline-chromium oxide composites, *J. Mater. Sci. Mater. Electron.* 25 (2014) 1237–1243. <https://doi.org/10.1007/s10854-014-1715-7>.
- [76] T. Chandrasekhar, N. Sasidhar, B. Chethan, Y.T. Ravikiran, Effect of chromium oxide in improving

- humidity sensing properties of polypyrrole/chromium oxide composite, AIP Conf. Proc. 2274 (2020) 020012. <https://doi.org/10.1063/5.0022613>.
- [77] S. Pokhrel, K.S. Nagaraja, Electrical and humidity sensing properties of Chromium(III) oxide-tungsten(VI) oxide composites, *Sensors Actuators, B Chem.* 92 (2003) 144–150. [https://doi.org/10.1016/S0925-4005\(03\)00251-X](https://doi.org/10.1016/S0925-4005(03)00251-X).
- [78] W. Daoping, C. Dandan, W. Lingling, W. Yuan, Q. Li, T. Wang, High performance humidity sensors based on CeO₂ nanoparticles, *Sensors Actuators B. Chem.* 215 (2015) 125–132. <https://doi.org/10.1016/j.snb.2015.03.051>.
- [79] H. Feng, C. Li, T. Li, F. Diao, T. Xin, B. Liu, Y. Wang, Three-dimensional hierarchical SnO₂ dodecahedral nanocrystals with enhanced humidity sensing properties, *Sensors Actuators B. Chem.* 243 (2017) 704–714. <https://doi.org/10.1016/j.snb.2016.12.043>.
- [80] J. Xu, K. Yu, J. Wu, D. Shang, L. Li, Y. Xu, Z. Zhu, Synthesis, field emission and humidity sensing characteristics of honeycomb-like CuO, *J. Phys. D. Appl. Phys.* 42 (2009) 075417. <https://doi.org/10.1088/0022-3727/42/7/075417>.
- [81] P.K. Kannan, R. Saraswathi, J.B.B. Rayappan, A highly sensitive humidity sensor based on DC reactive magnetron sputtered zinc oxide thin film, *Sensors Actuators, A Phys.* 164 (2010) 8–14. <https://doi.org/10.1016/j.sna.2010.09.006>.
- [82] X. Peng, J. Chu, B. Yang, P.X. Feng, *Sensors and Actuators B: Chemical* Mn-doped zinc oxide nanopowders for humidity sensors, *Sensors Actuators B. Chem.* 174 (2012) 258–262. <https://doi.org/10.1016/j.snb.2012.07.011>.
- [83] B.C. Yadav, R. Srivastava, C.D. Dwivedi, P. Pramanik, *Sensors and Actuators A: Physical* Synthesis of nano-sized ZnO using drop wise method and its performance as moisture sensor, *Sensors Actuators A.* 153 (2009) 137–141. <https://doi.org/10.1016/j.sna.2009.05.010>.
- [84] S. Rajarajan, G. Ramkumar, A comparative study of humidity sensing and photocatalytic applications of pure and nickel (Ni) -doped WO₃ thin films, *Appl. Phys. A.* 123 (2017) 401. <https://doi.org/10.1007/s00339-017-0983-5>.
- [85] V. Jadkar, A. Pawbake, R. Waykar, A. Jadhavar, A. Date, D. Late, H. Pathan, S. Gosavi, S. Jadkar, Synthesis of g-WO₃ thin films by hot wire-CVD and investigation of its humidity, *Phys. Status Solidi A.* 214 (2017) 1600717. <https://doi.org/10.1002/pssa.201600717>.

- [86] Z. Wang, L. Shi, F. Wu, S. Yuan, Y. Zhao, M. Zhang, The sol – gel template synthesis of porous TiO_2 for a high performance humidity sensor, *Nanotechnology*. 22 (2011) 275502. <https://doi.org/10.1088/0957-4484/22/27/275502>.
- [87] J. Wang, M. Su, J. Qi, L. Chang, Sensors and Actuators B : Chemical Sensitivity and complex impedance of nanometer zirconia thick film humidity sensors, *Sensors Actuators B Chem.* 139 (2009) 418–424. <https://doi.org/10.1016/j.snb.2009.03.070>.
- [88] Q. Qi, Y. Feng, T. Zhang, X. Zheng, G. Lu, Influence of crystallographic structure on the humidity sensing properties of KCl-doped TiO_2 nanofibers, *Sensors Actuators B Chem.* 139 (2009) 611–617. <https://doi.org/10.1016/j.snb.2009.03.041>.
- [89] W. Lin, C. Liao, T.-C. Chang, S.-H. Chen, R.-J. Wu, Humidity sensing properties of novel graphene/ TiO_2 composites by sol-gel process, *Sensors Actuators B. Chem.* 209 (2015) 555–561. <https://doi.org/10.1016/j.snb.2014.12.013>.
- [90] Z. Li, A.A. Haidry, B. Gao, T. Wang, Z. Yao, The effect of Co-doping on the humidity sensing properties of ordered mesoporous TiO_2 , *Appl. Surf. Sci.* 412 (2017) 638–647. <https://doi.org/10.1016/j.apsusc.2017.03.156>.
- [91] Z. Li, H. Zhang, W. Zheng, W. Wang, H. Huang, C. Wang, A.G. Macdiarmid, Y. Wei, D.U. V, V. Pennsylv, Highly Sensitive and Stable Humidity Nanosensors Based on LiCl Doped TiO_2 Electrospun Nanofibers, *J. Am. Ceram. Soc.* 130 (2008) 5036–5037.
- [92] K. Katayama, K. Hasegawa, Y. Takahashi, T. Akiba, H. Yanagida, Humidity Sensitivity of Nb_2O_5 -doped TiO_2 Ceramics, *Sensors Actuators A.* 24 (1990) 55–60.
- [93] H. Yin, J. Ni, W. Jiang, Z. Zhang, K. Yu, Synthesis , field emission and humidity sensing characteristics of monoclinic VO_2 nanostructures, *Phys. E.* 43 (2011) 1720–1725. <https://doi.org/10.1016/j.physe.2011.05.030>.
- [94] M.S. Pawar, P.K. Bankar, M.A. More, D.J. Late, Ultra-thin V_2O_5 Nanosheets Based Humidity Sensor, Photodetector and Its Enhanced Field Emission Properties, *RSC Adv.* 5 (2015) 88796–88804. <https://doi.org/10.1039/C5RA17253E>.
- [95] C. Xu, K. Miyazaki, Humidity sensor with manganese oxide for room temperature, *Sens. Actuators B.* 13–14 (1993) 523–524. [https://doi.org/https://doi.org/10.1016/S0925-4005\(97\)00330-4](https://doi.org/https://doi.org/10.1016/S0925-4005(97)00330-4).
- [96] V. Jeseentharani, A. Dayalan, K.S. Nagaraja, Co-precipitation synthesis, humidity sensing and

- photoluminescence properties of nanocrystalline Co^{2+} substituted zinc(II)molybdate ($\text{Zn}_{1-x}\text{Co}_x\text{MoO}_4$; $x = 0, 0.3, 0.5, 0.7, 1$), Solid State Sci. 67 (2017) 46–58. <https://doi.org/10.1016/j.solidstatesciences.2017.02.008>.
- [97] W. Qu, J.U. Meyer, Thick-film humidity sensor based on porous MnWO_4 material, Meas. Sci. Technol. 8 (1997) 593–600. <https://doi.org/10.1088/0957-0233/8/6/002>.
- [98] W. Qu, Wojtek Wlodarski, Jorg-Uwe Meyer, Comparative study on micromorphology and humidity sensitive properties of thin–film and thick–film humidity sensors based on semiconducting MnWO_4 , Sensors Actuators B Actuators. 64 (2000) 76–82. [https://doi.org/https://doi.org/10.1016/S0925-4005\(99\)00487-6](https://doi.org/10.1016/S0925-4005(99)00487-6).
- [99] S. Upadhyay, Humidity-sensitive characteristic of $\text{Ba}_{0.99}\text{La}_{0.01}\text{SnO}_3$, Phys. Status Solidi Appl. Mater. Sci. 205 (2008) 1113–1119. <https://doi.org/10.1002/pssa.200723006>.
- [100] H. Klym, A. Ingram, O. Shpotyuk, I. Hadzaman, O. Hotra, Y. Kostiv, Nanostructural Free-Volume Effects in Humidity-Sensitive $\text{MgO-Al}_2\text{O}_3$ Ceramics for Sensor Applications, J. Mater. Eng. Perform. 25 (2016) 866–873. <https://doi.org/10.1007/s11665-016-1931-9>.
- [101] K.I. Arshak, K. Twomey, Investigation into a novel humidity sensor operating at room temperature, Microelectronics J. 33 (2002) 213–220. [https://doi.org/10.1016/S0026-2692\(01\)00150-1](https://doi.org/10.1016/S0026-2692(01)00150-1).
- [102] M. Sabarilakshmi, K. Janaki, Effect of Mg concentration on structural, optical and humidity sensing performance of SnO_2 nanoparticles prepared by one step facile route, J. Mater. Sci. Mater. Electron. 28 (2017) 8101–8107. <https://doi.org/10.1007/s10854-017-6516-3>.
- [103] R. Sundaram, K.S. Nagaraja, Electrical and humidity sensing properties of lead(II) tungstate-tungsten(VI) oxide and zinc(II) tungstate-tungsten(VI) oxide composites, Mater. Res. Bull. 39 (2004) 581–590. <https://doi.org/10.1016/j.materresbull.2003.12.014>.
- [104] Y. Shimizu, H. Okada, Humidity-Sensitive Characteristics of Porous La-Ti-V-O Glass-Ceramics, J. Am. Ceram. Soc. 72 (1987) 51–53. [https://doi.org/https://doi.org/10.1111/j.1151-2916.1989.tb06149.x](https://doi.org/10.1111/j.1151-2916.1989.tb06149.x).
- [105] Q. Yuan, N. Li, W. Geng, Y. Chi, J. Tu, X. Li, C. Shao, Humidity sensing properties of mesoporous iron oxide/silica composite prepared via hydrothermal process, Sensors Actuators, B Chem. 160 (2011) 334–340. <https://doi.org/10.1016/j.snb.2011.07.057>.
- [106] A.M. Edwin Suresh Raj, C. Mallika, K. Swaminathan, O.M. Sreedharan, K.S. Nagaraja, Zinc(II) oxide-zinc(II) molybdate composite humidity sensor, Sensors Actuators, B Chem. 81 (2002) 229–236.

[https://doi.org/10.1016/S0925-4005\(01\)00957-1](https://doi.org/10.1016/S0925-4005(01)00957-1).

- [107] K. Hayat, F. Niaz, S. Ali, M.J. Iqbal, M. Ajmal, M. Ali, Y. Iqbal, Thermoelectric performance and humidity sensing characteristics of La_2CuO_4 nanofibers, *Sensors Actuators, B Chem.* 231 (2016) 102–109. <https://doi.org/10.1016/j.snb.2016.02.127>.
- [108] A.C. Caballero, M. Villegas, M. Viviani, M.T. Buscaglia, M. Leoni, Effect of humidity on the electrical response of porous BaTiO_3 ceramics, *J. Mater. Sci. Lett.* 18 (1999) 1297–1299. <https://doi.org/https://doi.org/10.1023/A:1006662805186>.
- [109] J.G. Kim, Electrical properties and fabrication of porous BaTiO_3 -based ceramics, *J. Mater. Sci. Lett.* 21 (2002) 477–479. <https://doi.org/10.1023/A:1015334623555>.
- [110] J. Yuk, T. Troczynski, Sol-gel BaTiO_3 thin film for humidity sensors, *Sensors Actuators, B Chem.* 94 (2003) 290–293. [https://doi.org/10.1016/S0925-4005\(03\)00371-X](https://doi.org/10.1016/S0925-4005(03)00371-X).
- [111] J. Wang, B.K. Xu, S.P. Ruan, S.P. Wang, Preparation and electrical properties of humidity sensing films of BaTiO_3 /polystyrene sulfonic sodium, *Mater. Chem. Phys.* 78 (2003) 746–750. [https://doi.org/10.1016/S0254-0584\(02\)00421-2](https://doi.org/10.1016/S0254-0584(02)00421-2).
- [112] J. Wang, H. Wan, Q. Lin, Properties of a nanocrystalline barium titanate on silicon humidity sensor, *Meas. Sci. Technol.* 14 (2003) 172–175. <https://doi.org/10.1088/0957-0233/14/2/303>.
- [113] B. Ertug, T. Boyraz, O. Addemir, Investigation of the electrical conductivity and humidity sensitivity characteristics of BaTiO_3 ceramics with PMMA additive, *Arch. Metall. Mater.* 57 (2012) 437–442. <https://doi.org/10.2478/v10172-012-0043-2>.
- [114] L. Wang, Y. He, J. Hu, Q. Qi, T. Zhang, DC humidity sensing properties of BaTiO_3 nanofiber sensors with different electrode materials, *Sensors Actuators, B Chem.* 153 (2011) 460–464. <https://doi.org/10.1016/j.snb.2010.11.016>.
- [115] J. Lu, L. Cheng, Y. Zhang, J. Huang, C. Li, Effect of the seed layer on surface morphology and humidity sensing property of CoTiO_3 nanocrystalline film, *Ceram. Int.* 43 (2017) 5823–5827. <https://doi.org/10.1016/j.ceramint.2017.01.080>.
- [116] R. Ganeshkumar, C.W. Cheah, R. Zhao, Annealing temperature and bias voltage dependency of humidity nanosensors based on electrospun KNbO_3 nanofibers, *Surfaces and Interfaces.* 8 (2017) 60–64. <https://doi.org/10.1016/j.surfin.2017.04.010>.
- [117] D. Li, J. Zhang, L. Shen, W. Dong, C. Feng, C. Liu, S. Ruan, Humidity sensing properties of SrTiO_3

- nanospheres with high sensitivity and rapid response, *RSC Adv.* 5 (2015) 22879–22883. <https://doi.org/10.1039/c5ra00451a>.
- [118] Y. Tian, M. Xu, P. Huang, E. Lei, H. Hao, C. Cui, The abnormal sensitivity and its mechanism of (Ba, Pb)TiO₃ semiconductor ceramics, *Chinese Sci. Bull.* 50 (2005) 936–939. <https://doi.org/10.1360/04we0107>.
- [119] Y.-C. Yeh, T.-Y. Tseng, D.-A. Chang, Electrical Properties Porous Titania Ceramic Humidity Sensors, *J. Am. Ceram. Soc.* 71 (1989) 1472–1475. [https://doi.org/https://doi.org/10.1111/j.1151-2916.1989.tb07679.x](https://doi.org/10.1111/j.1151-2916.1989.tb07679.x).
- [120] Z.A. Ansari, T.G. Ko, J.H. Oh, Humidity sensing behavior of thick films of strontium-doped lead-zirconium-titanate, *Surf. Coatings Technol.* 179 (2004) 182–187. [https://doi.org/10.1016/S0257-8972\(03\)00820-X](https://doi.org/10.1016/S0257-8972(03)00820-X).
- [121] M. Ahmadipour, M.F. Ain, Z.A. Ahmad, Effect of thickness on surface morphology, optical and humidity sensing properties of RF magnetron sputtered CCTO thin films, *Appl. Surf. Sci.* 385 (2016) 182–190. <https://doi.org/10.1016/j.apsusc.2016.05.098>.
- [122] J. Wang, B. Xu, G. Liu, J. Zhang, T. Zhang, Improvement of nanocrystalline BaTiO₃ humidity sensing properties, *Sensors Actuators, B Chem.* 66 (2000) 159–160. [https://doi.org/10.1016/S0925-4005\(00\)00308-7](https://doi.org/10.1016/S0925-4005(00)00308-7).
- [123] A. Kazemzadeh, F.A. Hessary, N. Jafari, New solid state sensor for detection of humidity, based on Ni, Co, and Mn oxide nano composite doped with Lithium, *Sensors Transducers J.* 94 (2008) 161–169.
- [124] L. Jingbo, L. Wenchao, Z. Yanxi, W. Zhimin, Preparation and characterization of Li⁺-modified Ca_{0.9}Pb_{0.1}TiO₃ film for humidity sensor, *Sensors Actuators, B Chem.* 75 (2001) 11–17. [https://doi.org/10.1016/S0925-4005\(00\)00686-9](https://doi.org/10.1016/S0925-4005(00)00686-9).
- [125] A. Bonavita, A. Caddemi, N. Donato, P. Accordino, S. Galvagno, G. Neri, U. Messina, C. Sperone, S. Agata, U. Messina, C. Sperone, S. Agata, Electrical characterization and modeling of thin-film humidity sensors, in: *Proc. IEEE Conf. Electron. Circuits Syst. ICECS 2001*, Sept. 2–5, Malta, 2001: pp. 673–676. <https://doi.org/10.1109/ICECS.2001.957565>.
- [126] D. Depla, S. Mahieu, J.E. Greene, Sputter Deposition Processes, in: P.M. Martin (Ed.), *Handb. Depos. Technol. Film. Coatings*, 3rd ed., Elsevier Inc, Oxford, 2010: pp. 253–296. <https://doi.org/https://doi.org/10.1016/B978-0-8155-2031-3.00005-3>.

- [127] M.T. Johnson, C.B. Carter, J. Michael, SEM Analysis of Oxide Thin Films and Reactions, *J. Am. Ceram. Soc.* 82 (1999) 1644–1646. <http://dx.doi.org/10.1111/j.1151-2916.1999.tb01981.x>.
- [128] S. Nasrazadani, S. Hassani, Modern analytical techniques in failure analysis of aerospace, chemical, and oil and gas industries, in: A.S.H. Makhlof, M. Aliofkhazraei (Eds.), *Handb. Mater. Fail. Anal. with Case Stud. from Oil Gas Ind.*, 1st ed., Butterworth Heinemann, Oxford, 2016: pp. 39–54. <https://doi.org/10.1016/B978-0-08-100117-2.00010-8>.
- [129] D. Bell, A. Garratt-Reed, *Energy Dispersive X-ray Analysis in the Electron Microscope*, 1st ed., BIOS Scientific Publishers Limited, Oxford, 2003. <https://doi.org/10.4324/9780203483428>.
- [130] N.P. Barradas, C. Jeynes, S.M. Jackson, NOM RBS / Simulated annealing analysis of buried SiCO₂ layers formed by implantation of O into cubic silicon carbide, *Nucl. Instruments Methods Phys. Res. B.* 136–138 (1998) 1168–1171. [https://doi.org/10.1016/S0168-583X\(97\)00686-1](https://doi.org/10.1016/S0168-583X(97)00686-1).
- [131] M.H. Herman, Applications of Rutherford backscattering spectrometry to refractory metal silicide characterization, *J. Vac. Sci. Technol. B* 2. 748 (1984). <https://doi.org/10.1116/1.582873>.
- [132] N.P. Barradas, C. Pascual-Izarra, Double scattering in RBS analysis of PtSi thin films on Si, *Nucl. Instruments Methods Phys. Res. B.* 228 (2005) 378–382. <https://doi.org/10.1016/j.nimb.2004.10.074>.
- [133] N.P. Barradas, M.A. Reis, Accurate calculation of pileup effects in PIXE spectra from first principles, *X-RAY Spectrosc.* 35 (2006) 232–237. <https://doi.org/10.1002/xrs.903>.
- [134] Y. Waseda, E. Matsubara, K. Shinoda, *X-ray Diffraction Crystallography: Introduction, Examples and Solved Problems*, 1st ed., Springer, Berlin, 2011. <https://doi.org/10.1007/978-3-642-16635-8>.
- [135] M.K. Gupta, N. Sinha, B. Kumar, Synthesis and Comparative Study of ZnO Nanorods for Structural , Optical and Dielectric Behaviour, *Integr. Ferroelectr.* 118 (2010) 61–66. <https://doi.org/10.1080/10584587.2010.489478>.
- [136] P.R.N. Childs, *Practical Temperature Measurement*, 1st ed., Butterworth-Heinemann, Oxford, 2001. <https://doi.org/10.1016/B978-0-7506-5080-9.X5000-X>.
- [137] L.C. Fernandes, D.M. Correia, N. Pereira, C.R. Tubio, S. Lanceros-Méndez, Highly Sensitive Humidity Sensor Based on Ionic Liquid–Polymer Composites, *ACS Appl. Polym. Mater.* 1 (2019) 2723–2730. <https://doi.org/10.1021/acsapm.9b00675>.
- [138] A.D. Smith, K. Elgammal, F. Niklaus, A. Delin, A.C. Fischer, S. Vaziri, F. Forsberg, M. Räsander, H.

- Hugosson, L. Bergqvist, S. Schröder, S. Kataria, M. Östling, M.C. Lemme, Resistive graphene humidity sensors with rapid and direct electrical readout, *Nanoscale*. 7 (2015) 19099–19109. <https://doi.org/10.1039/c5nr06038a>.
- [139] T. Elangovan, P. Kuppusami, R. Thirumurugesan, V. Ganesan, E. Mohandas, D. Mangalaraj, Nanostructured CrN thin films prepared by reactive pulsed DC magnetron sputtering, *Mater. Sci. Eng. B Solid-State Mater. Adv. Technol.* 167 (2010) 17–25. <https://doi.org/10.1016/j.mseb.2010.01.021>.
- [140] K. Ibrahim, M.M. Rahman, X. Zhao, J.P. Veder, Z. feng Zhou, E. Mohammadpour, R.H. Majeed, A.N. Nikoloski, Z.T. Jiang, Annealing effects on microstructural, optical, and mechanical properties of sputtered CrN thin film coatings: Experimental studies and finite element modeling, *J. Alloys Compd.* 750 (2018) 451–464. <https://doi.org/10.1016/j.jallcom.2018.04.012>.
- [141] V. Uvarov, I. Popov, Metrological characterization of X-ray diffraction methods at different acquisition geometries for determination of crystallite size in nano-scale materials, *Mater. Charact.* 85 (2013) 111–123. <https://doi.org/10.1016/j.matchar.2013.09.002>.
- [142] X. Pang, K. Gao, F. Luo, H. Yang, L. Qiao, Y. Wang, A.A. Volinsky, Annealing effects on microstructure and mechanical properties of chromium oxide coatings, *Thin Solid Films*. 516 (2008) 4685–4689. <https://doi.org/10.1016/j.tsf.2007.08.083>.
- [143] C.K. Chung, A. Nautiyal, T.S. Chen, Y.L. Chang, Grain boundary scattering for temperature coefficient of resistance (TCR) behaviour of Ta-Si-N thin films, *J. Phys. D. Appl. Phys.* 41 (2008) 185404 (5pp). <https://doi.org/10.1088/0022-3727/41/18/185404>.
- [144] G.S. Chung, W.J. Lee, J.S. Song, Characteristics of chromium nitride thin-film strain gauges, *Sensors Mater.* 13 (2001) 013–023.
- [145] J.H. Tyan, J.T. Lue, Grain boundary scattering in the normal state resistivity of superconducting NbN thin films, *J. Appl. Phys.* 75 (1994) 325–331. <https://doi.org/10.1063/1.355853>.
- [146] M.A. Park, K. Savran, Y.J. Kim, Weak localization and the Mooij rule in disordered metals, *Phys. Status Solidi Basic Res.* 237 (2003) 500–512. <https://doi.org/10.1002/pssb.200301654>.
- [147] Y.M. Blanter, V.M. Vinokur, L.I. Glazman, Weak localization in metallic granular media, *Phys. Rev. B - Condens. Matter Mater. Phys.* 73 (2006) 165322. <https://doi.org/10.1103/PhysRevB.73.165322>.
- [148] S. Srinivas, S.N. Kaul, S.N. Kane, Enhanced electron-electron interaction, weak localization and electron-magnon scattering contributions to electrical resistivity in Fe- and Co-based metallic glass wires, *J. Non.*

Cryst. Solids. 248 (1999) 211–223. [https://doi.org/10.1016/S0022-3093\(99\)00144-1](https://doi.org/10.1016/S0022-3093(99)00144-1).

- [149] A.F. Mayadas, M. Shatzkes, Electrical-resistivity model for polycrystalline films: The case of arbitrary reflection at external surfaces, *Phys. Rev. B.* 1 (1970) 1382–1389. <https://doi.org/10.1103/PhysRevB.1.1382>.
- [150] R. Sanjiñs, M. Benkahoul, C.S. Sandu, P.E. Schmid, F. Lvy, Relationship between the physical and structural properties of Nb₅Si₃N₈ thin films deposited by dc reactive magnetron sputtering, *J. Appl. Phys.* 98 (2005) 123511. <https://doi.org/10.1063/1.2149488>.
- [151] K.S. Karimov, K.Y. Cheong, M. Saleem, I. Murtaza, M. Farooq, A.F. Mohd Noor, Ag/PEPC/NiPc/ZnO/Ag thin film capacitive and resistive humidity sensors, *J. Semicond.* 31 (2010) 054002. <https://doi.org/10.1088/1674-4926/31/5/054002>.
- [152] S. Wang, H. Lin, H. Bor, Y. Tsai, C. Wei, Characterization of chromium thin films by sputter deposition, *J. Alloys Compd.* 509 (2011) 10110–10114. <https://doi.org/10.1016/j.jallcom.2011.08.052>.
- [153] R. Mientus, R. Grötschel, K. Ellmer, Optical and electronic properties of CrO_xN_x films, deposited by reactive DC magnetron sputtering in Ar/N₂/O₂(N₂O) atmospheres, *Surf. Coatings Technol.* 200 (2005) 341–345. <https://doi.org/10.1016/j.surfcoat.2005.02.181>.
- [154] R. Arvinte, J. Borges, R.E. Sousa, D. Munteanu, N.P. Barradas, E. Alves, F. Vaz, L. Marques, Preparation and characterization of CrN_xO_x thin films: The effect of composition and structural features on the electrical behavior, *Appl. Surf. Sci.* 257 (2011) 9120–9124. <https://doi.org/10.1016/j.apsusc.2011.05.109>.
- [155] J. Lin, Z.L. Wu, X.H. Zhang, B. Mishra, J.J. Moore, W.D. Sproul, A comparative study of CrN_x coatings Synthesized by dc and pulsed dc magnetron sputtering, *Thin Solid Films.* 517 (2009) 1887–1894. <https://doi.org/10.1016/j.tsf.2008.09.093>.
- [156] P. Carvalho, F. Vaz, L. Rebouta, L. Cunha, C.J. Tavares, C. Moura, E. Alves, A. Cavaleiro, P. Goudeau, E. Le Bourhis, J.P. Riviere, J.F. Pierson, O. Banakh, Structural, electrical, optical, and mechanical characterizations of decorative ZrO_xN_x thin films, *J. Appl. Phys.* 98 (2005) 023715. <https://doi.org/10.1063/1.1990261>.
- [157] J. Inoue, H. Asami, M. Hirai, T. Suzuki, H. Suematsu, W. Jiang, K. Yatsui, Oxidation properties of Cr(N,O) thin films synthesized by pulsed laser deposition, in: S. Miyake (Ed.), *Nov. Mater. Process. by Adv. Electromagn. Energy Sources*, 1st ed., Elsevier Science, Osaka, 2005: pp. 203–207. <https://doi.org/10.1016/B978-008044504-5/50041-6>.

- [158] T. Suzuki, H. Saito, M. Hirai, H. Suematsu, W. Jiang, K. Yatsui, Preparation of $\text{Cr}(\text{N}_x\text{O}_y)$ thin films by pulsed laser deposition, *Thin Solid Films*. 407 (2002) 118–121. [https://doi.org/10.1016/S0040-6090\(02\)00023-8](https://doi.org/10.1016/S0040-6090(02)00023-8).
- [159] R. Wang, L.L.H. King, A.W. Sleight, Highly conducting transparent thin films based on zinc oxide, *J. Mater. Res.* 11 (1996) 1659–1664. <https://doi.org/10.1557/JMR.1996.0208>.